The translational landscape of SARS-CoV-2 and infected cells

Maritza Puray-Chavez[1,*], Kasyap Tenneti[1,*], Hung R. Vuong[1,*], Nakyung Lee[1,*], Yating Liu[2], Amjad Horani[3], Tao Huang[4], Sean P. Gunsten[4], James B. Case[5], Wei Yang[2], Michael S. Diamond[1,5,6], Steven L. Brody[4], Joseph Dougherty[2,7], Sebla B. Kutluay[1]

[1] Department of Molecular Microbiology, Washington University School of Medicine, Saint Louis, MO 63110, USA

[2] Department of Genetics, Washington University School of Medicine, Saint Louis, MO 63110, USA

[3] Department of Pediatrics, Allergy, Immunology and Pulmonary Medicine, Washington University School of Medicine, Saint Louis, MO 63110, USA

[4] Department of Medicine, Pulmonary and Critical Care Medicine, Washington University School of Medicine, Saint Louis, MO 63110, USA

[5] Department of Medicine, Infectious Disease Division, Washington University School of Medicine, Saint Louis, MO 63110, USA

[6] Department of Pathology & Immunology, Washington University School of Medicine, Saint Louis, MO 63110, USA

[7] Department of Psychiatry, Washington University School of Medicine, Saint Louis, MO 63110, USA

Correspondence: Kutluay@wustl.edu

Highlights

- Ribo-seq reveals key translationally regulated events in SARS-CoV-2 replication
- SARS-CoV-2 frameshifting is substantially more efficient than HIV-1
- SARS-CoV-2 infection results in transcriptional upregulation of inflammatory and interferon-stimulated genes
- SARS-CoV-2 disarms host responses at the level of mRNA translation

Summary

SARS-CoV-2, a betacoronavirus with a positive-sense RNA genome, has caused the ongoing COVID-19 pandemic. Although a large number of transcriptional profiling studies have been conducted in SARS-CoV-2 infected cells, little is known regarding the translational landscape of host and viral proteins. Here, using ribosome profiling in SARS-CoV-2-infected cells, we identify structural elements that regulate viral gene expression, alternative translation initiation events, as well as host responses regulated by mRNA translation. We found that the ribosome density was low within the SARS-CoV-2 frameshifting element but high immediately downstream, which suggests the utilization of a highly efficient ribosomal frameshifting strategy. In SARS-CoV-2-infected cells, although many chemokine, cytokine and interferon stimulated genes were upregulated at the mRNA level, they were not translated efficiently, suggesting a translational block that disarms host innate host responses. Together, these data reveal the key role of mRNA translation in SARS-CoV-2 replication and highlight unique mechanisms for therapeutic development.

KEYWORDS: SARS-CoV-2, ribosome profiling, ribo-seq, mRNA translation, virus replication, ribosomal frameshifting, virus-host interaction, immune response, translational repression

INTRODUCTION

The Coronavirus (CoV) group encompasses of a number of single-stranded, positive-sense RNA viruses with unusually large genomes (27-32 kb), which infect a wide range of animal species, including humans (Masters, 2006, Weiss and Navas-Martin, 2005). Previously, outbreaks of two members of this group, severe acute respiratory syndrome (SARS-CoV) and Middle East respiratory syndrome (MERS-CoV), have caused lethal respiratory illnesses in 2002 and 2012, respectively (de Wit et al., 2016). Presently, SARS-CoV-2, the causative agent of the ongoing Coronavirus Disease-2019 (COVID-19) pandemic, has infected millions of people worldwide and has devastated the global economy. Currently, there are limited options for antiviral or immunomodulatory treatment against SARS-CoV-2, with only few therapies being currently recommended for more severe COVID-19 cases. A basic understanding of the replicative mechanisms of SARS-CoV-2 and associated host responses potentially can foster the development of virus-specific therapies.

The first two-thirds of the 5' end of the SARS-CoV-2 genome is composed of two overlapping open reading frames (ORFs), ORF1a and ORF1b, which encode for two polyproteins, pp1a and pp1ab (Nakagawa et al., 2016). Pp1a is produced when translation of the genomic RNA terminates at the stop codon of ORF1a. Pp1ab is generated via a programmed -1 ribosomal frameshift (PRF) that occurs at the overlap between ORF1a and ORF1b, permitting the elongating ribosomes to bypass the termination signal in ORF1a (Plant and Dinman, 2008). Following synthesis, pp1a and pp1ab are cleaved by viral proteases to generate 15-16 mature nonstructural proteins (nsp) (Nakagawa et al., 2016). Many proteins encoded in ORF1b, are part the replication complex, thus making the -1 PRF to generate pp1ab a critical translational event for SARS-CoV-2 replication. Frameshifting in coronaviruses is regulated by a highly conserved heptanucleotide

slippery sequence (UUUAAAC) and an RNA pseudoknot structure a few nucleotides downstream (Plant and Dinman, 2008). The current models of PRF suggest that ribosomes stall upon encountering the pseudoknot (Plant et al., 2003, Korniy et al., 2019). This event presumably enhances the efficiency of ribosomal frameshifting by forcing the ribosomes to pause on the slippery sequence, which in turn promote the -1 slippage. Once the pseudoknot unwinds and resolves, the ribosome goes on to translate the alternate ORF.

Another well-known frameshifting mechanisms in human viruses is employed by retroviruses through a stem-loop structure that regulates the expression of Gag/Gag-Pol transcripts (Jacks et al., 1988, Wilson et al., 1988). Frameshifting here is thought essential for maintenance of the ratio of Gag and Gag-Pol polyproteins as well as viral infectivity (Shehu-Xhilaga et al., 2001, Garcia-Miranda et al., 2016). While frameshifting is thought to be highly inefficient in HIV-1, with only 5-10% of ribosomes continuing into the Pol ORF (Baril et al., 2003, Dulude et al., 2006, Jacks et al., 1988), CoV frameshifting is thought to occur at a much higher efficiency (Irigoyen et al., 2016). However, to date, the behavior of ribosomes within the frameshifting element for neither SARS-CoV-2 nor HIV-1 in infected cells has been empirically assessed.

In addition to hijacking the host translational machinery, SARS-CoV-2 can modulate host mRNA translation so as to suppress the immune system to ensure efficient propagation. Indeed, several viral proteins reportedly impair host gene expression post-transcriptionally (Lokugamage et al., 2012, Xiao et al., 2008, Kopecky-Bromberg et al., 2006, Huang et al., 2011, Zhou et al., 2008, Kamitani et al., 2009, Narayanan et al., 2008, Nakagawa et al., 2016). SARS-CoV nonstructural protein nsp1 induces endonucleolytic cleavage in the 5'-UTR of cellular mRNAs, accelerating their turnover, but not in viral mRNAs (Kopecky-

130 Bromberg et al., 2006). Furthermore, nsp1 tightly binds to the 40S ribosomal subunit and
131 blocks translation initiation (Kamitani et al., 2009). This dual capacity to cleave host
132 mRNAs and directly inhibit their translation may allow SARS-CoV-2 to overcome the type
133 I IFN response in infected cells, as has been demonstrated for SARS-CoV (Narayanan et
134 al., 2008). On the other hand, the bulk of published research on SARS-CoV- and SARS-
135 CoV-2-host interactions has relied on transcriptional profiling to study the immune
136 response to infection (Blanco-Melo et al., 2020, Butler et al., 2020, Menachery et al., 2014,
137 Mitchell et al., 2013, Wilk et al., 2020, Zhou et al., 2020). Such approaches may not fully
138 capture the host immune response to infection, in the face of viral mechanisms that block
139 host mRNA translation.
140
141 Here, we have conducted in-depth ribosome profiling studies to gain insight into the role
142 of translational regulation in SARS-CoV-2 replication and the resulting host responses.
143 We found that ribosome occupancy on viral mRNAs was temporally regulated and partly
144 dependent on RNA abundance. In addition, ribosomes engaged with novel translation
145 initiation sites (TIS) and other potential regulatory elements on SARS-CoV-2 RNAs. Viral
146 mRNAs encoding E, S and ORF1ab were more efficiently translated than other viral
147 mRNAs, but the overall translation efficiency of viral mRNAs was not substantially different
148 than cellular mRNAs. In addition, we found that ribosomes were depleted rather than
149 enriched on the SARS-CoV-2 frameshifting site and SARS-CoV-2 frameshifting was more
150 efficient than HIV-1. Remarkably, while numerous inflammatory chemokines, cytokines
151 and ISGs were upregulated transcriptionally in SARS-CoV-2-infected cells, we found that
152 many were not efficiently translated. Overall, our study defines the translational landscape
153 of SARS-CoV-2-infected cells, revealing novel events that may promote viral replication
154 and disarm host immune responses at the level of mRNA translation.
155

156 **RESULTS**

157

158 ***Ribosome profiling reveals key features of SARS-CoV-2 translational program***

159 To study the relationship between transcriptionally and translationally regulated events at
160 early and late phases of SARS-CoV-2 infection, Vero E6 cells infected at low and high
161 multiplicity of infection (MOIs, 0.1 and 2 plaque forming units [PFU]/cell, respectively))
162 were monitored by RNA-seq and ribo-seq during the course of infection (**Fig. 1A**). Viral
163 antigen staining of infected cells revealed that the majority of the cells were infected by 24
164 hpi for low MOI and by 12 hpi for high MOI infections (**Fig. S1A, S1B**). High quality
165 duplicate sequencing libraries with favorable mapping statistics were generated (**Tables**
166 **S1-S4)**. The quality of each ribo-seq library was assessed as follows. First, the length of
167 distribution of ribo-seq reads that mapped to cellular and viral transcriptomes were within
168 the expected range of ribosome protected fragments (**Fig. S2A, S2B, S3A, S3B**) (Ingolia
169 et al., 2012, Ingolia et al., 2009). We noted that in one experiment read lengths trended to
170 be longer likely due to lesser extent of nuclease digestion (**Fig. S3A, B**). Second, the
171 majority of ribo-seq reads mapped to coding sequences and 5' UTRs, with clear reduction
172 in the fraction of reads mapping to 3'UTRs when compared to RNA-seq experiments done
173 in parallel (**Fig. S2C, Fig. S4**). Third, mapped ribosome footprints within the CDSs were
174 enriched in fragments that align to the translated frame (**Fig. S2D, Fig. S5**).

175

176 For low MOI infections, ~50% of the uniquely mapping RNA-seq reads were derived from
177 SARS-CoV-2 mRNAs by 24 hours post infection (hpi) (**Fig. 1B**). By 48 hpi >80% of the
178 uniquely mapping reads were viral (**Fig. 1B**) demonstrating that viral mRNAs quickly
179 dominate the total cellular mRNA pool. The percentage of SARS-CoV-2-derived mRNAs
180 did not increase further at 72 hpi (**Fig. 1B**), partly due to virus-induced cytotoxicity.
181 Comparatively, a smaller percentage of ribosome-associated mRNAs were derived from

182 SARS-CoV-2, approximating 20 to 40% at early and late time points in infection,
183 respectively (**Fig. 1C**). Despite their relative abundance in the cytosol, viral RNAs were
184 not specifically enriched in ribosome-bound pool. As we observed significant levels of
185 cytotoxicity at 72 hpi, we focused our analyses on the earlier 24 and 48 hpi time points.
186
187 Plotting of RNA-seq reads on the viral genome demonstrated that N-derived sgRNAs were
188 highly abundant throughout infection (**Fig. 1D-E, and S5**), a finding consistent with
189 previous RNA-seq studies (Kim et al., 2020, Huang et al., 2020). Expectedly, the majority
190 of these reads were derived from positive sense viral mRNAs, albeit substantially lower
191 copies of anti-sense transcripts were also detectable (**Fig. S6**). Furthermore, ribosomes
192 were enriched on N mRNAs, with a high peak surrounding the translation start site, at 24
193 hpi (**Fig. 1D**). As expected from the low abundance of ORF10 encoding sgRNAs, we noted
194 that ribosome occupancy fell abruptly after the N stop codon, although footprints were still
195 detectable within the ORF10 coding sequence with an average read count of 136 per
196 nucleotide, A second high ribosome occupancy site was observed within the M ORF at 24
197 hpi, again with a distinct peak around the translation start site (**Fig. 1D**). ORFs downstream
198 from S also were bound by ribosomes, albeit at lower levels (**Fig. 1D**). By 48 hpi, we found
199 that high ribosome occupancy sites shifted from the N ORF to upstream ORFs, and
200 numerous high ribosome occupancy sites were observed throughout the viral RNAs (**Fig.**
201 **1E**). In particular, at 48 hpi, ORF1a and ORF1b translation appeared to be more efficient,
202 considering the low level of mRNA abundance observed by RNA-seq (**Fig. 1E and S7B**).
203 Ribosome occupancy within ORF1a and ORF1b was non-uniform and did not correlate
204 with proteolytic cleavage events occurring within these polyproteins (**Fig. S7A-B**).
205 Ribosome footprints were also observed on antisense transcripts (**Fig. S8**), albeit fairly
206 infrequently and with read length distributions not matching those expected from ribosome
207 protected fragments (**Fig. S2E**).

208

209 Similar to other CoVs, SARS-CoV-2 frameshifting is thought to be mediated by the
210 conserved heptanucleotide slippery sequence (UUUAAAC) and a RNA pseudoknot
211 downstream from it spanning nucleotides 13408-13540 (**Fig. 1F**). Of note, ribosome
212 occupancy was fairly low within the frameshifting site but increased immediately following
213 it (**Fig. 1G**), suggesting a relatively high efficiency of frameshifting. Length distribution of
214 reads that mapped to ORF1ab was similar to other virally mapping reads (**Fig. S2F**) and
215 within the expected range of ribosome-protected fragments. Average ribosome density
216 within ORF1b was modestly lower, and comparison of ribosome densities between ORF1a
217 and ORF1b revealed a frameshifting efficiency of %63 (+/- 3%), in line with published
218 reports of frameshifting efficiency with SARS-CoV-2 as well as other coronaviruses
219 (Irigoyen et al., 2016, Dinan et al., 2019, Finkel et al., 2020). In addition, we noted that
220 ribosome density was also depleted ~100 nucleotides upstream of the frameshifting site
221 (**Fig. 1G**). Based on this, we speculate that the pseudoknot structure may sterically hinder
222 translating ribosomes upstream of the frameshifting site or that the RNA structure may
223 extend to upstream sequences.

224

225 ***Kinetics of early translationally regulated events in SARS-CoV-2 replication***

226 To identify early translationally regulated events in SARS-CoV-2 replication, we conducted
227 similar experiments in Vero E6 cells infected at a higher MOI but monitored at earlier times
228 in infection (**Fig. 1A, S1B**). At 2 hpi, only a small fraction of mRNAs was derived from
229 SARS-CoV-2 RNAs, though by 12 hpi, nearly 80% of the total mRNA pool was viral (**Fig.**
230 **2A**). Viral RNAs were more abundant in the ribosome bound pool at 2 hpi and by 12 hpi
231 ~50% of the ribosome-protected fragments contained viral sequences (**Fig. 2B**). As
232 before, viral RNAs did not appear to be specifically enriched in the ribosome-bound pool
233 (**Fig. 2B**).

234

235 N-derived sequences were the most abundant viral RNA species throughout the infection
236 (**Fig. 2C-G**) and consistent results were obtained from replicate experiments (**Fig. S9-**
237 **S10**). Analysis of ribosome footprints on viral RNAs at 2 hpi revealed the presence of a
238 high occupancy site (**Fig. 2C, Fig. S11A, and S12A**), which accounted for the majority of
239 ribo-seq reads derived from viral RNAs (**Fig. 2B**). This region, spanning nucleotides
240 27371-27457 is located between ORF6 and ORF7, is not fully conserved between SARS-
241 CoV-2 and SARS-CoV (**Fig. S13A**), and is predicted to form a structured hairpin loop with
242 high probability (**Fig. S13B**). Reads that mapped to this region displayed a length
243 distribution around 29-34 nt, suggesting that they are authentic ribosome protected
244 fragments rather than aberrant products of PCR or digestion bias. High ribosome
245 occupancy in this region was maintained throughout the infection (**Fig. S13C**) and across
246 biological replicates (**Fig. S11A and S12A**).

247

248 Following a high MOI infection, ribosome occupancy on viral RNAs increased significantly
249 by 6 hpi, featuring N and M coding mRNAs constituting as the most frequently translated
250 RNAs (**Fig. 2D, Fig. S11B, and S12B**). Ribosome occupancy across viral RNAs increased
251 further by 12 hpi (**Fig. 2E, S11C and S12C**) and remained high during the remainder of
252 infection (**Fig. 2F, 2G, S11D, S11E, S12D and S12E**). Ribosome footprints were non-
253 uniform with numerous high and low frequency binding sites observed reproducibly across
254 viral RNAs (**Fig. 2C-G, S11, S12**). Of note, the frameshifting element had a generally low
255 ribosome density compared to the surrounding sequences throughout the infection (**Fig.**
256 **S14A-E**). Ribosome occupancy was low upstream of the frameshifting site (**Fig. S14A-E**),
257 again suggesting the possibility of an alternative RNA structure and/or steric hindrance by
258 the frameshifting element on translating ribosomes. Once again, read length distribution
259 ribo-seq reads mapping to ORF1ab was similar to other virally mapping reads **(Fig. S14F**

260 **vs. Fig. S3B).** Comparison of read density distribution between ORF1a and ORF1b
261 indicated a relatively high efficiency of frameshifting ranging from %75 to %100 throughout
262 the course of infection **(Fig. S14G).**
263
264 Analogous to SARS-CoV-2, HIV-1 also utilizes -1 ribosomal frameshifting, in this case for
265 generation of the Gag-Pol polyprotein (Jacks et al., 1988, Wilson et al., 1988). HIV-1
266 frameshifting is regulated by a slippery sequence followed by a structured hairpin loop
267 (Mouzakis et al., 2013, Staple and Butcher, 2005). To compare the frameshifting efficiency
268 of SARS-CoV-2 to HIV-1, we next performed paired ribo-seq and RNA-seq experiments
269 in HIV-1-infected CD4+ T-cells isolated from two independent donors (**Table S5 and S6**).
270 Length distribution of ribo-seq derived reads that mapped to cellular (**Fig. S15A**) and viral
271 (**Fig. S15B**) mRNAs were within the expected range of ribosome-protected fragments. In
272 addition, ribo-seq reads that mapped to cellular mRNAs had a 3-nt periodicity in frame
273 with annotated CDSs (**Fig. S15C**) and were largely depleted off of 3' UTRs (**Fig. S15D**),
274 highlighting the high quality of the ribo-seq experiments.
275
276 We found that, in contrast to SARS-CoV-2, ribosome occupancy was high within the HIV-
277 1 frameshifting element (**Fig. S16B**) but dropped substantially 3' to it and remained low
278 throughout the Pol ORF (**Fig. S16A and 16C**). This suggests that ribosomes may pause
279 and accumulate within the frameshifting site but only a small fraction of them continue
280 translating into the Pol ORF, a finding that agrees with prior estimates of low (5-10%) HIV-
281 1 frameshifting efficiency (Biswas et al., 2004, Dulude et al., 2006, Shehu-Xhilaga et al.,
282 2001, Baril et al., 2003, Jacks et al., 1988). Thus, we conclude that programmed ribosomal
283 frameshifting is regulated through distinct mechanisms between HIV-1 and SARS-CoV-2,
284 despite the similar structural elements that regulate this process.
285

286 We next tested whether SARS-CoV-2 can utilize alternative translation initiation, which is
287 increasingly recognized as a key post-transcriptional regulatory mechanism (Kwan and
288 Thompson, 2019, James and Smyth, 2018). To do so, ribo-seq experiments were
289 performed as in Fig. 2 but in the presence of harringtonine, which results in the
290 accumulation of ribosomes at translation initiation sites. In addition to accumulation of
291 ribosomes at the canonical start codons, harringtonine treatment resulted in accumulation
292 of ribosomes at alternative translation initiation sites during the course of infection, albeit
293 at generally lower frequencies. For example, at 6 hpi, an internal noncanonical start codon
294 'UUG' within M ORF was utilized at ~30% of the time, predicted to result in an out-of-frame
295 peptide of 53 amino acids long (**Table S7**). An alternative translation initiation codon 'AGG'
296 at 21868 nt appeared to be utilized within S at 6, 12 and 24 hpi, which would result in a
297 short 18 amino acid peptide (**Table S7**). Finally alternative translation initiation sites were
298 observed within M, resulting in an out-of-frame peptide and a truncated version of M
299 (**Table S7**). Together, these results provide the high resolution map of ribosomes on viral
300 mRNAs during different stages of infection and reveal key sequence and structural
301 elements that may influence SARS-CoV-2 translational program.
302
303 ***Ribo-seq in primary HBECs reveal a similar SARS-CoV-2 translational program***
304 To corroborate these findings in a more relevant cell culture system, we performed ribo-
305 seq studies in primary human bronchial epithelial cells (HBEC) grown at air-liquid
306 interface. Cells inoculated at an MOI of 0.5 were processed for RNA-seq and ribo-seq at
307 6, 24, 48 and 72 hpi. A parallel set of experiments were done at MOI of 1 and followed
308 during a shorter time course. In contrast to Vero cells, the progression of infection in
309 HBECs was relatively slow and a small percentage of the cells were infected by 24 hpi
310 (not shown). Despite some donor-to-donor variation (as expected from primary cell culture
311 models), SARS-CoV-2 spread was visible by 72 hpi as evident in the presence of

312 numerous infection foci (**Fig. S17A**). By 96 hpi, a large fraction of ciliated cells expressing
313 ACE2 were infected (**Fig. S17B, S17C**). These findings were largely corroborated upon
314 infection of HBECs with a NeonGreen reporter virus (Xie et al., 2020) (**Fig. S17D**). In line
315 with this, the amount of newly synthesized viral RNAs was low at 6 hpi, although by 24 hpi
316 numerous virally derived sequences (as assessed by RNA-seq) were present (**Table S8**
317 **and S9**). Similar to experiments done in Vero E6 cells (**Fig. 1 and 2**), the majority of these
318 sequences were derived from subgenomic viral mRNAs coding for N and to a lesser extent
319 upstream ORFs including M, ORF6, ORF7 and ORF8 (**Fig. 3A**). As with previous
320 experiments, length distribution of ribo-seq reads mapping to cellular and viral mRNAs
321 matched the size expected from ribosome-protected fragments (**Fig. S18A**), most ribo-
322 seq reads mapped to CDSs and 5' UTRs but not 3' UTRs (**Fig. S18B**) and were enriched
323 in fragments that align to the translated frame (**Fig. S19**), highlighting the high quality of
324 ribo-seq libraries. The lower permissiveness of these cells to infection resulted in few viral
325 RNAs bound to ribosomes at 6 hpi (**Table S8**). Ribosomes bound by viral RNAs were
326 readily detected at 24, 48, and 72 hpi, with N and M ORFs being the most frequently
327 translated (**Fig. 3B-D**). We found distinct accumulation of ribosomes within N, M and
328 ORF1a translation start sites as well as 5' end of ORF1a (**Fig. 3B-D**). Overall, these results
329 suggest the presence of a similar gene expression cascade in the primary HBECs in
330 comparison to Vero E6 cells.
331
332 ***Inflammatory and innate immune mRNAs are inefficiently translated in SARS-CoV-***
333 ***2 infected cells***
334 Several studies have focused on the transcriptional landscape of innate responses to
335 SARS-CoV-2 (Blanco-Melo et al., 2020, Butler et al., 2020, Menachery et al., 2014,
336 Mitchell et al., 2013, Wilk et al., 2020, Zhou et al., 2020). However, currently there is little
337 evidence as to whether transcriptionally induced mRNAs are actually translated in the

338 setting of a virus that can in principle induce translational arrest (Nakagawa et al., 2016)
339 and ISGs (e.g. IFIT1 and PKR) that can inhibit mRNA translation (Li et al., 2015). Using
340 ribo-seq, we next assessed how cells respond to SARS-CoV-2 infection at a translational
341 level.
342
343 Paired RNA-seq and ribo-seq data (for high MOI infections of Vero E6 cells) obtained from
344 independent and reproducible experiments (**Fig. S20**) were analyzed for differential gene
345 expression patterns. As early as 2 hpi, we found transcriptional upregulation of several
346 chemokine ligands (i.e.CXCL1, CXCL3, CXCL8) and transcription factors involved in cell
347 cycle regulation and induction of inflammation (i.e.NR4A3 and EGR3) (**Fig. 4A, S21A,**
348 **S22A**). In contrast, we noted a general trend in RNA downregulation (**Fig. 4A**), which
349 persisted throughout the infection (**Fig. 4B-C, and S23**). 6 hpi timepoint was also marked
350 by upregulation of chemokine ligands (CXCL1, CXCL3, CXCL8, CXCL11) (**Fig. 4B, S21A,**
351 **S22A**) and by 12 hpi numerous ISGs (e.g. IFIT family members, MX1, IFI44), IL1A and
352 IFN-λ were also upregulated (**Fig. 4C, S21A, S22A**). Remarkably, the majority of these
353 transcript level changes were not apparent in Ribo-seq data (**Fig. 4D-F and S21A, S22A**),
354 suggesting that mRNAs encoding genes in the host defense responses may not be
355 efficiently translated. Of note, this pattern was not global. For example, EGR1, EGR3 and
356 IFIH1, were induced at equivalent levels both in RNA-seq and ribo-seq experiments (**Fig.**
357 **S24**). This pattern grossly continued at 24 and 48 hpi, though by 48 hpi upregulated genes
358 were primarily associated with cell death, likely reflecting viral and immune-mediated
359 cytotoxicity (**Fig. S21, S22, S25**).
360
361 Time-course gene set enrichment analysis corroborated the differences between
362 transcriptional and translational responses in infected Vero cells. For example, numerous
363 sets of genes involved in chemokine, cytokine and interferon signaling were upregulated

364 at 2 hpi in the RNA-seq data set (**Fig. 5A**), but these changes were not evident in the ribo-
365 seq data set (**Fig. 5B**). Although at later time points both RNA-seq and ribo-seq data sets
366 were enriched in gene sets related to interferon responses, inflammatory responses, IL2
367 and IL6 signaling, these responses appeared to be lower in magnitude for ribo-seq data,
368 with fewer genes enriched in each family and a significant delay in kinetics (**Fig. 5A-B**).
369 Together, these findings suggest that immune response genes are translationally
370 repressed and their expression significantly delayed in infected cells.
371
372 Many of these findings held consistent for the low MOI infections. Analysis of independent
373 and reproducible RNA-seq (**Fig. S26A**) and Ribo-seq (Fig. **S26B**) experiments revealed
374 that transcription factors ATF3 and EGR1, key regulators of inflammatory responses, were
375 upregulated at 24 hpi alongside with numerous chemokine ligands (i.e. CXCL1, CXCL8,
376 CXCL10) and interleukin 6 (**Fig. 6A**). Of note, despite the fact that Vero cells are known
377 to be deficient in type-I IFN production, we noted the upregulation of numerous ISGs (i.e.
378 IFIT1, IFIT2, IFIT3) as well as IFN-lambda at 24 hpi (**Fig. 6A**). The 48 hpi timepoint was
379 marked by upregulation of genes involved in cell cycle regulation and apoptosis (i.e. FOS,
380 NR4A3), as well as inflammatory cytokines such as IL-31 and ISGs including OASL (**Fig.**
381 **6B**). In line with our above observations, the great majority of the transcriptionally
382 upregulated genes were not translationally upregulated at 24 hpi (**Fig. 6C**) and 48 hpi
383 (**Fig.6D**). Interleukins IL11 and IL1A stood out as immune-related genes that were
384 translationally upregulated at 24 and 48 hpi, respectively (**Fig. 6C, D**)
385
386 Although a small percentage of cells in the primary airway culture system described above
387 were infected, analysis of differentially expressed transcripts revealed significant and
388 consistent trends in gene expression profiles upon infection. For example, we found that
389 gene sets involved in inflammatory response, interferon alpha, interferon gamma, IL2 and

390 IL6 signaling were upregulated as early as 6 hpi by RNA-seq, despite the lack of
391 observable virus replication (**Fig. S27A**). At 48 hpi, the transcriptional landscape was
392 marked by the upregulation of other sets of genes involved in IL2 and IL6 signaling,
393 inflammation, complement and hypoxia, amongst others (**Fig. S27A**). Many of these
394 responses were tuned down or non-existent in the ribo-seq data set (**Fig. S27B**),
395 suggesting that mRNA translation may similarly be repressed in this more relevant cell
396 culture system.
397
398 ***Comparison of SARS-CoV-2 and host mRNA translation efficiencies***
399 We next assessed the translational efficiency of cellular host response genes in infected
400 cells and how this compared to viral mRNA translation. In mock-infected cells, most
401 cellular mRNAs were translated at levels proportional to their mRNA abundance (**Fig. 7A**).
402 Notable outliers included mRNAs encoding for ribosomal subunits, which were translated
403 less efficiently as observed before (Riba et al., 2019), and DDX25 RNA helicase, which
404 constituted one of the most efficiently translated mRNAs (**Fig. 7A**). The translational
405 efficiency of viral mRNAs was not substantially different than the majority of cellular
406 mRNAs with ORF1AB, S and E mRNAs translated at a modestly higher efficiency and the
407 remainder of viral mRNAs at a lower efficiency than average, a pattern that did not vary
408 with progression of infection (**Fig. 7B-F**). Thus, the high abundance of viral mRNAs, as
409 opposed to a specific regulated mechanism, likely ensures the abundance of viral proteins.
410 Consistent with our earlier observations, we found that the differentially expressed
411 chemokine ligands and ISGs generally were translated less efficiently (**Fig. 7C-D and**
412 **S14**). Of note numerous cellular genes with unknown functions were translationally
413 upregulated in infected cells (**Fig. 7B-F**).
414
415 **DISCUSSION**

416 Here we utilized ribosome profiling (ribo-seq) coupled with RNA-seq to study the
417 translational events that regulate viral gene expression and host responses over the
418 course of SARS-CoV-2 infection. SARS-CoV-2 replicates rapidly, with viral RNAs
419 constituting the great majority of the total mRNA pool soon after infection. Our data show
420 that viral mRNA abundance is the main determinant of viral protein expression and SARS-
421 CoV-2 mRNAs sequester ribosomes from the translating pool by competition, simply
422 outnumbering the host counterparts. Notwithstanding certain viral mRNAs (i.e. those
423 encoding S, E and ORF1ab) were translated modestly more efficiently translated than
424 others. While the overall conclusions are similar, another study found that ORF1ab was
425 less efficiently translated compared with other viral mRNAs (Finkel et al., 2020), which we
426 ascribe to possible differences in read depth (with our study having substantially higher
427 read depth within ORF1ab), RNA-seq approaches and infection conditions (5-7 hpi in
428 (Finkel et al., 2020) vs. a more extensive time course analysis done in our study). In
429 addition, we show that ribosome occupancy on viral RNAs is uneven, changes during the
430 course of infection, and alternative translation initiation sites and RNA structural elements
431 may be utilized. Analysis of mRNA translation in infected cells uncovered that
432 inflammatory and innate responses can be dampened by inefficient mRNA translation in
433 SARS-CoV-2 –infected cells. Together, our study provides an in-depth picture of
434 translationally regulated events in SARS-CoV-2 replication and reveal that impairment of
435 host mRNA translation may allow SARS-CoV-2 to evade host immunity.
436
437 We observed that, in contrast to HIV-1, SARS-CoV-2 RNA employs a highly efficient
438 frameshifting strategy to facilitate virus replication. Ribosomal frameshifting requires a
439 heptanucleotide slippery sequence and a RNA pseudoknot, generally a H-type, positioned
440 six to eight nucleotides downstream (Giedroc and Cornish, 2009). Multiple models for
441 ribosomal frameshifting posit that the ribosome pauses at the slippery sequence upon

442 encountering the pseudoknot, which is resistant to unwinding (Farabaugh, 1996, Dinman,
443 2012). While paused, ribosomes either stay in-frame or slip -1 nt before resuming
444 translation. A corollary of this notion is that the stimulatory structure, in turn, enhances
445 frameshifting efficiency by promoting ribosomal pausing. In line with this, we observed low
446 ribosome occupancy in the SARS-CoV-2 frameshifting site (**Fig. 1G and S14**). Notably,
447 ribosome pausing extended 100 nucleotides upstream of the frameshifting site,
448 suggesting an alternative frameshifting structure that includes upstream sequences or
449 steric hindrance imposed by the pseudoknot structure. Ribosome density downstream of
450 the frameshifting site within the ORF1b was remarkably high, suggesting high efficiency
451 of frameshifting in spite of ribosomal pausing.

452 The behavior of ribosomes was drastically different between the SARS-CoV-2 and HIV-1
453 frameshifting sites. In contrast to SARS-CoV-2, ribosomes accumulated within the HIV-1
454 frameshifting element and only a small fraction of them continued into the Pol ORF,
455 suggesting a significantly lower efficiency of frameshifting. We hypothesize that both
456 sequence-specific and structural features contribute to SARS-CoV-2 frameshifting
457 efficiency. It is thought that HIV-1 has a particularly slippery sequence (UUUUUUA) as
458 compared to SARS-CoV-2 (UUUAAAC), which may underlie this difference (Giedroc and
459 Cornish, 2009). In addition, structures downstream of the slippery sequence may have an
460 impact (Plant and Dinman, 2008). For example, the HIV-1 frameshifting element is
461 predicted to have a simpler pseudoknot (Chang et al., 1999, Parkin et al., 1992, Brierley
462 and Dos Ramos, 2006, Huang et al., 2014) or hairpin loop structure (Mouzakis et al., 2013,
463 Staple and Butcher, 2005). In particular, previous studies suggest that frameshifting
464 efficiency positively correlates with the mechanical stability and thermodynamic stability
465 of the pseudoknot and stem loop, respectively (Hansen et al., 2007, Chen et al., 2009,
466 Bidou et al., 1997). In addition, host proteins can also affect frameshifting. Of note, an

467 interferon-stimulated gene (ISG) product, known as C19orf66 (Shiftless), has recently
468 been demonstrated to impair HIV-1 replication through inhibition of HIV-1 programmed
469 frameshifting (Wang et al., 2019). Altogether, our data suggest that SARS-CoV-2 and HIV-
470 1 frameshifting occurs through distinct mechanisms. It remains to be determined how
471 distinct elements within the frameshifting site affect and whether other viral or cellular
472 proteins are involved in modulating the frameshifting efficiencies of these viruses.

473 SARS-CoV-2 mRNA translation may be regulated by other structural elements. For
474 example, we observed a high ribosome occupancy site that is present throughout the
475 course of infection and located between ORF6 and ORF7 (**Fig. 2C, S13**). This site is
476 computationally predicted to form a structured hairpin loop that may trigger ribosomal
477 pausing during translation of subgenomic viral RNA and thus lead to the observed high
478 ribosome occupancy (**Fig. S8**). Of note, ribosome occupancy within this region fell after
479 harringtonine treatment, suggesting that it may serve a function other than translation
480 initiation (not shown). While the biological role of this RNA structure is not apparent, it may
481 play a role in regulating the relative expression of ORF6 and ORF7 likely within the context
482 of viral subgenomic mRNAs. Other potential functions of this element include co-
483 translational protein folding, protein targeting, or co-translational degradation of both
484 mRNA and nascent peptide following pausing.
485

486 In addition, our study demonstrates that alternative, non-canonical translational start sites
487 internal to several viral genes such as S, E and M, can result in truncated isoforms or short
488 peptides (**Table S7**). While their presence still needs to be validated, this raises the
489 question of whether viral protein isoforms may play important biological role during
490 infection. SARS-CoV-2 infection also induced significant increase in utilization of canonical
491 as well as non-canonical translation initiation sites from numerous cellular mRNAs (**Table**

492 **S10**), including members of the S100 family with known roles in inflammation (Bettum et
493 al., 2014, Li et al., 2020) and virus replication (Bharadwaj et al., 2013, Liu et al., 2015,
494 Taylor et al., 2018). These findings together emphasize the potential role of translationally
495 regulated events that may help shape viral replication and host responses to pathogens,
496 which may be overlooked in transcriptomics approaches.
497
498 Our study provides the first in depth picture of how host cell responses to SARS-CoV-2
499 are regulated at a post-transcriptional level. This is of utmost importance given that several
500 SARS-CoV proteins have been reported to suppress host translation and that numerous
501 genes involved in innate immunity act to block mRNA translation. Such regulatory events
502 would be completely neglected in transcriptomic screens. In fact, we observed
503 upregulation of proinflammatory chemokines as early as 2 hpi followed by a more delayed
504 induction of ISGs, a finding in line with previous observations in immortalized lung cell
505 lines (Blanco-Melo et al., 2020). However, the increase in transcript abundance did not
506 correlate with higher levels of translation and majority of them appeared to be translated
507 at a low efficiency (**Fig. 7**).
508
509 The apparent low translation efficiency of host response mRNAs may be mediated by the
510 SARS-CoV-2 protein nsp1, which was recently reported to associate tightly with the 40S
511 ribosomal subunit as well as non-translating 80S ribosomes to prevent binding of capped
512 mRNA and thus inhibit the formation of the translation initiation complex (Schubert et al.,
513 2020), much like its SARS-CoV counterpart (Narayanan et al., 2015). In addition, there is
514 increasing evidence that ectopic expression of Nsp1 can alter host mRNA translation (Rao
515 et al., 2020). Our study complements these studies and provides the first published
516 evidence on the potential inhibitory effects of Nsp1 on host mRNA translation at
517 biologically relevant infection settings. We cannot rule out that the observed translational

518 suppression may also be contributed by the host's attempt to curb viral replication,
519 including members of the IFIT family with known functions in translation inhibition (Hyde
520 and Diamond, 2015, Fensterl and Sen, 2015, Reynaud et al., 2015, Daffis et al., 2010,
521 Diamond and Farzan, 2013). A further alternative is that the translation of these mRNAs
522 is inherently inefficient due to presence of unique 5' UTR structures. Finally, it is plausible
523 that the relatively lower read depths obtained from ribo-seq libraries may have precluded
524 accurate assessment of differential gene expression changes. However, we think that this
525 is unlikely given the high level of mRNA expression for numerous innate immune genes
526 (based on RNA-seq) and the statistical models utilized herein to assess translational
527 suppression. Notwithstanding, future studies are warranted to empirically test these
528 possibilities and define the mechanism of apparent innate immune suppression.
529
530 While COVID-19 pathogenesis is in part due to virus-induced destruction of infected cells,
531 elevated production of inflammatory mediators and the virus-induced immunopathology
532 are thought to play a big role in SARS-CoV-2-induced lung injury (Channappanavar and
533 Perlman, 2017, Perlman and Dandekar, 2005). Our findings suggest that immune
534 responses in actively infected cells may be dampened or delayed for SARS-CoV-2 to
535 efficiently replicate and release viral progeny. As such, it is possible that the elevated
536 levels of inflammatory mediators in vivo is due to infection of immune cell subsets, such
537 as monocytes and macrophages, that are less permissive to SARS-CoV-2 but can sense
538 and respond to infection by secretion of immune modulatory molecules (Jafarzadeh et al.,
539 2020).
540
541 Taken together, we provide novel insight into and a rich resource on how translational
542 regulation shapes SARS-CoV-2 replication and host responses. Our finding that induction
543 of inflammatory and innate immune responses can be limited at the level of mRNA

544 translation provides a paradigm shifting mechanism of how SARS-CoV-2 can encounter
545 immune responses. Modulation of viral RNA structures and proteins that regulate mRNA
546 translation will undoubtedly provide a unique avenue for therapeutic development.
547
548 **ACKNOWLEDGEMENTS:** We would like to thank members of the Diamond lab for
549 reagents and support. This work was supported by Washington University startup funds
550 for SBK, R21 AI145669 to SBK and JD, National Science Foundation Graduate Research
551 Fellowship under Grant No. DGE-1745038 to KV, Stephen I. Morse postdoctoral
552 fellowship to MPC, Helen Hay Whitney Foundation postdoctoral fellowship to J.B.C., and
553 the Dorothy R. and Hubert C. Moog Professorship to SLB. All NGS data (48 sets of ribo-
554 seq and 48 sets of matching RNA-seq) are deposited in the GEO database under
555 GSE158930.
556
557 **AUTHOR CONTRIBUTIONS:** MPC, HRV, AH, TH, SGP, JBC conducted the experiments.
558 KT, NL, YL, WY conducted the bioinformatics analysis. HRV and SBK wrote the original
559 manuscript with input from MSD, SLB, JD, JBC.
560
561 **FIGURE LEGENDS**
562 **Figure 1. Ribo-seq reveals uneven ribosome occupancy on SARS-CoV-2 RNAs**
563 **during low MOI infection.** (A) Schematic diagram of Ribo-seq and RNA-seq experiments
564 conducted in this study. Vero E6 cells were infected at 0.1 pfu/cell and cells were
565 processed for RNA-seq and Ribo-seq at 24, 48 and 72 hpi. (B, C) Percentage of RNA-seq
566 (B) and Ribo-seq (C) reads uniquely mapping to SARS-CoV-2 and cellular transcripts at
567 the indicated time points post infection. Individual data points indicate biological replicates.
568 (D, E) Ribo-seq and RNA-seq reads (counts) along the viral genome at 24 hpi (D) and 48
569 hpi (E). Schematic diagram of SARS2 genome features shown below is co-linear. Red

570 arrows denote translation initiation sites. (F) Predicted secondary structure of the
571 frameshifting site is depicted. (G) Ribo-seq read counts at 48hpi within the SARS2
572 frameshifting site. The position of the frameshifting element is indicated with the red
573 rectangle.
574
575 **Figure 2. Changes in ribosome occupancy on the SARS-CoV-2 genome during high**
576 **MOI infection.** Vero E6 cells were infected at 2 pfu/cell and processed for RNA-seq and
577 Ribo-seq at 2, 6, 12, 24 and 48 hpi. (A, B) Percentage of RNA-seq (A) and Ribo-seq (B)
578 reads uniquely mapping to SARS-CoV-2 and cellular transcripts at the indicated time
579 points post-infection. Individual data points indicate biological replicates. (C-G) Ribo-seq
580 and RNA-seq reads (counts) mapping to the viral genome at 2 hpi (C), 6 hpi (D), 12 hpi
581 (E), 24 hpi (F) and 48 hpi (G) are shown. Schematic diagram of SARS2 genome features
582 illustrated below in co-linear.
583
584 **Figure 3. Ribo-seq experiments in primary HBEC cultures grown at ALI.** HBECs
585 grown at ALI were infected with SARS-CoV-2 at a MOI of 0.5 i.u./cell and processed for
586 RNA-seq at 24 hpi (A) and ribosome profiling at 24 (B), 48 (C) and 72 (D) hpi. Ribo-seq
587 reads (counts, y-axis) along the viral genome (x-axis) is shown. Schematic diagram of
588 SARS2 genome features shown below is co-linear.
589
590 **Figure 4. Differentially transcribed and translated host genes in SARS-CoV-2-**
591 **infected cells (high MOI).** Vero E6 cells were infected at 2 pfu/cell and processed for
592 RNA-seq at 2 hpi and Ribo-seq at 2 hpi (A, D), 6 hpi (B, E), and 12 hpi (C, F). Heatmaps
593 show the $\log_2$ counts per million mapped reads (cpm) of the top differentially expressed
594 genes (FDR<0.05, fold change>2) derived from two independent experiments. Scale of
595 each graph is shown below.

596

597 **Figure 5. Expression dynamics of differentially transcribed cellular mRNAs in**
598 **response to SARS-CoV-2 infection.** Time-course gene set analysis (TcGSA) was
599 performed on the RNA-seq (A) and Ribo-seq (B) data derived from the above experiments.
600 The heatmap shows an under (blue) or an over (red) expression for each significant gene
601 set. The numbers next to each gene set indicate a particular subset of genes which trend
602 differently from other genes within the same gene set.

603

604 **Figure 6. Differentially transcribed and translated host genes in SARS-CoV-2-**
605 **infected cells (low MOI).** Vero E6 cells were infected at 0.1 pfu/cell and cells were
606 processed for RNA-seq (A, B) and Ribo-seq (C, D) at 24 and 48 hpi. Heatmaps show the
607 counts per million mapped reads (cpm) of the top differentially expressed genes
608 (FDR<0.05, fold change>2) derived from two independent experiments. Scale of each
609 graph is shown below.

610

611 **Figure 7. Comparison of SARS-CoV-2 and host mRNA translation efficiencies.**
612 Translation efficiencies of viral and host mRNAs were assessed as described in Materials
613 and Methods. Plots show translational efficiencies of host mRNAs in mock infected cells
614 (A), 2 (B), and 48hpi (C) as these samples all had low or zero viral replication, as well as
615 viral and host mRNAs in infected cells at 6 hpi (C), 12 hpi (D) and 24 hpi (E). Translational
616 efficiencies of key differentially expressed genes derived from RNA-seq and Ribo-seq are
617 represented by orange circles. Reference genes with notably high and low translational
618 efficiencies are represented by blue circles. Viral genes are represented by red circles.

619

620

621

622 **MATERIALS AND METHODS**

623 **Chemicals and reagents.** Standard laboratory chemicals were obtained from reputable
624 suppliers such as Sigma-Aldrich. Cycloheximide (CHX) was obtained from Sigma,
625 dissolved in ethanol and stored at -20°C. Harringtonine (HT) was purchased from LKT
626 Laboratories, Inc., resuspended in DMSO and stored in aliquots of 2 mg/mL at -20°C.

627

628 **Plasmids and viruses.** A proviral plasmid encoding the full length HIV-1 genome was
629 obtained from NIH AIDS Reagents. HIV-1 stocks were generated by transfection of
630 Human embryonic kidney cell line, HEK293T, with proviral plasmids and collection of cell
631 culture supernatants two days after. Viruses were treated by DNase to avoid plasmid
632 carryover and concentrated by Lenti-X concentrator. HIV-1 stocks were titered on TZM-bl
633 cells by conventional methods. $CD4^+$ T-cells activated for 4-5 days were used for HIV-1
634 infections. SARS-CoV-2 strain 2019-nCoV/USA-WA1/2020 was obtained from Natalie
635 Thornburg at the Centers for Disease Control and Prevention (CDC), propagated in Vero
636 CCL-81 cells and titrated on Vero E6 cells by plaque-forming assays.

637

638 **Cells and infections.** HEK293T and TZM-bl cells were obtained from ATCC and NIH
639 AIDS Reagent Program respectively and were maintained in Dulbecco's Modified Eagle's
640 Medium (DMEM) (high glucose), supplemented with 10% fetal bovine serum (FBS) in a
641 humidified incubator at 37°C with 5% CO_2. For isolation of primary $CD4^+$ T-cells, buffy
642 coats (from anonymous healthy blood donors from Mississippi Blood Center) were
643 separated by Ficoll and $CD4^+$ T-cells purified using RosetteSep Human CD4+ T-cell
644 enrichment kit (STEMCELL Technologies). $CD4^+$ T-cells cells were maintained in Roswell
645 Park Memorial Institute 1640 medium (RPMI) supplemented with 10% heat-inactivated
646 FBS and L-glutamine. Activation of $CD4^+$ T cells was achieved by addition of 25 U/ml of
647 interleukin-2 (IL-2) and $CD4^+$ T-cell activation Dynabeads (Life Technologies). $CD4^+$ T-

648 cells activated for 4-5 days were used for HIV-1 infections. Vero CCL-81 and Vero E6
649 were cultured in DMEM supplemented with 10% FBS and 10 mM HEPES pH 7.4. For
650 SARS-CoV-2 infections, Vero E6 cells were incubated with SARS-CoV-2 inoculum in
651 DMEM-supplemented with 2% FBS for an hour in a humidified incubator at 37°C, after
652 which the initial inoculum was removed and replaced by cell culture media.
653
654 Primary human bronchial epithelial cells (HBECs) grown at air-liquid interface (ALI).
655 Human airway epithelial cells were isolated from surgical excess of tracheobronchial
656 segments of lungs donated for transplantation as previously described and were exempt
657 from regulation by US Department of Health and Human Services regulation 45 Code of
658 Federal Regulations Part 46 (Horani et al., 2012). Tracheobronchial cells were expanded
659 in culture, seeded on supported membranes (Transwell; Corning, Inc.), and differentiated
660 using ALI conditions as detailed before (You et al., 2002, Horani et al., 2018).
661
662 **Immunofluorescence.** Infected Vero E6 cells and HBECs were fixed with 4%
663 paraformaldehyde for 20 min at room temperature, followed by permeabilization using
664 0.5% Tween-20 in PBS for 10 min. Cells were blocked with 1% bovine serum albumin
665 (BSA) and 10% FBS in 0.1% Tween-20 PBS (PBST) for 1 h prior to staining with a rabbit
666 polyclonal anti SARS-CoV-2 nucleocapsid antibody (Sino Biological Inc. catalog # 40588-
667 T62) diluted 1:500 and incubated overnight at 4°C. The following day, cells were stained
668 with an Alexa Fluor 488-conjugated goat anti-rabbit secondary antibody (Invitrogen) at
669 1:1000 dilution, counter-stained with DAPI and imaged by microscopy.

670 *RNA in situ hybridization.* Primary-culture human airway epithelial cells were fully
671 differentiated at air-liquid interface on supported plastic membranes (Transwell, Corning).
672 Cells were fixed by immersion of the Transwell membrane in methanol:acetone (50:50%

673 volume) at -20 °C for 20 min followed by 4% paraformaldehyde at room temperature for
674 15 min. Cells were washed three times with phosphate buffered saline (PBS) and stored
675 at 4 °C. Prior to probing for vRNA, membranes containing cells were cut from plastic
676 supports, divided into 4 pieces, and placed in a fresh 48-well plate. RNA detection was
677 performed using the manufacturer protocol for RNAscope fluorescent in situ hybridization
678 (RNAscope Multiplex Fluorescent v2 Assay kit, Advanced Cell Diagnostics). Briefly, cells
679 on membranes were treated with 3% hydrogen peroxide for 10 min at room temperature,
680 washed with distilled water, then treated with protease III solution, diluted 1:15 in PBS, for
681 10 min in a humidified hybridization oven at 40 °C. The cells were then washed with PBS
682 and incubated for 2 hr at 40 °C with manufacturer designed anti-sense probes specific for
683 SARS-CoV-2 positive strand S gene encoding the spike protein (RNAscope Probe-V-
684 nCoV2019-S, cat# 848561) or ORF1ab (RNAscope Probe-V-nCoV2019-orf1ab-O2-
685 sense-C2 cat # 854851-C2). The probes were visualized according to the manufacturers'
686 instructions by incubation with RNAscope amplifiers, horseradish peroxidase, and
687 fluorescent label (Opal fluorophores, Perkin-Elmer). Membranes were mounted on glass
688 slides using anti-fade medium containing DAPI (Fluoroshield, Sigma-Aldrich). Images
689 were obtained using a 5000B Leica microscope equipped with a charge-coupled device
690 camera (Retiga 200R) interfaced with QCapture Pro software (Q Imaging).
691
692 **Ribosome profiling.** Ribosome profiling (Ribo-seq) was performed as described before
693 with the following modifications (Ingolia et al., 2009, Ingolia et al., 2012). Mock- and HIV-
694 1- or SARS-CoV-2-infected cells were treated with complete cell culture media
695 supplemented with 0.1 mg/mL CHX for 1 min at room temperature followed by one round
696 of wash in ice-cold PBS supplemented with 0.1 mg/mL CHX. Cells were lysed in 1X
697 mammalian polysome lysis buffer (20 mM Tris·HCl (pH 7.4), 150 mM NaCl, 5 mM $MgCl_2$,
698 1% Triton X-100, 0.1% NP-40, 1 mM DTT, 10 units of DNase I, with 0.1 mg/mL CHX). The

699 cells were then triturated by repeated pipetting and incubated with lysis buffer for at least
700 20 min to ensure virus inactivation. Lysates were centrifuged for 10 min at ≥20,000 g at
701 4°C for clarification. The supernatants were split into multiple aliquots, with SDS added to
702 one aliquot to a final concentration of 1% for downstream RNA-seq sample preparation,
703 and flash frozen in a 70% ethanol/dry ice bath or directly placed at -80°C. Lysates were
704 treated with RNase I (5U/OD_{260}) and ribosome-protected fragments were isolated via
705 centrifugation through Microspin S-400 HR columns (GE Healthcare) and purified using
706 the RNA Clean and Concentrator kit (Zymo Research). Recovered ribosome-bound
707 fragments (RBFs) are then subjected to rRNA depletion using RiboZero beads from the
708 TruSeq Stranded Total RNA Library Prep Gold kit (Illumina) and purified using Zymo RNA
709 Clean and Concentrator kit. Fragments were then end-labeled with γ-^{32}P-ATP using T4
710 polynucleotide kinase (NEB), separated on 15% TBE-Urea gels and visualized by
711 autoradiography. RNA fragments of ~30 nt were excised from the gels and purified as
712 detailed before in 400 µL of 0.4 M NaCl supplemented with 4 µL SUPERaseIN. 3' and 5'
713 adapters were sequentially ligated as in a previously described protocol (Kutluay et al.,
714 2014, Kutluay and Bieniasz, 2016), reverse transcribed and PCR amplified. Libraries were
715 then sequenced on HiSeq-2000 or NextSeq 500 platforms (Illumina) at the Genome
716 Technology Access Center or the Edison Family Center for Genome Sciences & Systems
717 Biology, respectively, at Washington University School of Medicine. All ribo-seq and RNA-
718 seq data were deposited on GEO database under GSE158930.
719
720 **RNA-seq.** An aliquot of cell lysates harvested from ribosome profiling (Ribo-seq)
721 experiments above was processed in parallel for RNA-seq using TruSeq Stranded mRNA
722 library prep (Illumina) following extraction using Zymo RNA-Clean and Concentrator (5)
723 kit. RNA-seq libraries were constructed using TruSeq RNA single-index adapters and
724 deep sequenced as above at Washington University in St. Louis.

725

726 **Data analysis.** All of the data analysis pipelines used in this study are deposited to GitHub
727 under kutluaylab. Below we detail the salient steps of data analyses:

728

729 ***Mapping.*** Generated RNA-seq and Ribo-seq data were analyzed by publicly available
730 software and custom scripts. In brief, for Ribo-seq, reads were separated based on
731 barcodes and the adapters trimmed using BBDuk (http://jgi.doe.gov/data-and-
732 tools/bb-tools/) and FastX Toolkit (http://hannonlab.cshl.edu/fastx_toolkit/). The
733 resulting reads were mapped to the viral genome/transcriptome using the Bowtie aligner
734 (Langmead et al., 2009) (mapping criteria -v 1, -m 10), and to the African green monkey
735 (AGM) genome (*Chlorocebus sabaeus*) in STAR (Dobin et al., 2013) (mapping criteria
736 FilterMismatchNoverLmax 0.04). For AGM alignments, reads were first mapped to rRNA
737 to remove any rRNA-derived reads not completely removed by depletion kits and to the
738 SARS-CoV-2 genome to remove virally derived reads. The remaining reads were then
739 mapped to the AGM genome. RNA-seq reads were similarly mapped to the viral and AGM
740 genomes using STAR, although the rRNA alignment step was omitted. For AGM
741 alignments, mapped reads were annotated using the featureCounts package and GTF
742 files freely available from NCBI and Ensembl.

743

744 ***Statistical Analysis:*** Differential gene expression analysis was carried out using the
745 featureCounts output files via the edgeR package (Robinson et al., 2010), available from
746 Bioconductor. Considering that virally derived sequences quickly dominated the host
747 mRNA pool, for differential gene expression of host mRNAs, library sizes were normalized
748 relative to reads that map only to host mRNAs. Efforts in this area focused on determining
749 upregulated genes using individual Ribo-seq and RNA-seq experiments, as well as the

750 analysis of log_2-fold change differences between Ribo-seq and RNA-seq to discover
751 translationally regulated genes. These same files and packages were also used to
752 generate quality control plots and graphics highlighting differentially expressed genes.
753 The calculation of translational efficiency involved normalizing counts to account for library
754 size in edgeR to generate log2 counts-per-million (log_2CPM) estimates for each gene in
755 Ribo-seq and RNA-seq, and subtracting log2CPM RNA-seq from log_2CPM Ribo-seq to
756 provide an estimate of the difference in expression level between Ribo-seq and RNA-seq
757 for a given gene.
758
759 Additionally, the R package TcGSA was used to determine individual host genes and gene
760 sets differentially regulated over time (Hejblum et al., 2015). The normalized gene counts
761 at each time-point were provided as input, along with the 'hallmark' Gene Matrix file
762 containing annotated sets of processes and associated genes, downloaded from GSEA
763 (Subramanian et al., 2005, Mootha et al., 2003). As output, TcGSA provides clusters of
764 genes within each gene set, which follow particular trends. From these clusters, individual
765 genes differentially regulated over time were extracted and plotted as heatmaps in R.
766
767 Downstream analysis of sets of differential genes involved the use of goseq (Young et al.,
768 2010) and KEGGREST R packages (Tenenbaum, 2020). Annotations of 5'UTRs, CDSs
769 and 3'UTRs were retrieved and repetitive low-complexity elements were removed. The R
770 package riboWaltz (Lauria et al., 2018) was utilized to determine the location of ribosomal
771 P-sites with respect to the 5' and 3' end of reads, as well as illustrating triplet periodicity
772 and determining the percentage of reads within each frame in CDS and UTR . Finally, the
773 metagene R package (Beauparlant, 2020) was applied to generate an aggregate analysis
774 of ribosomal density downstream of start codons and upstream of stop codons in the
775 corresponding genome.

776

777 Alternative TIS sites in both host and viral reads were found using the Ribo-TISH package
778 (Zhang et al., 2017). For viral TIS, analysis was carried out in the 'predict' mode comparing
779 samples mock-treated or treated with harringtonine at each timepoint (with replicates).
780 This was replicated for host analysis, although with the additional step of analysis in the
781 'diff' mode to predict TIS differentially regulated between infected and uninfected cells.

782

783 ***Viral Counts:*** Viral read density plots were generated using the SAM file from viral
784 genome alignment. The SAMtools (Li et al., 2009) package was used to create an mpileup
785 file containing information about the read density, strandedness, mapping quality, and
786 nucleotide identity at each position. Custom scripts (deposited at GitHub under
787 kutluaylab) then were utilized to create files providing only the nucleotide identity and
788 number of counts at each position for both sense and antisense reads. These were then
789 visualized by scripts written in R.

790

791 As SARS-CoV-2 generates chimeric subgenomic mRNAs (sgRNAs) in addition to its
792 genomic RNA (gRNA), featureCounts could not be used to accurately estimate viral gene
793 counts from RNASeq due to the presence of nested 3' sequences. Therefore, in order to
794 visualize and enumerate such chimeric sequences the BWA aligner (Li and Durbin, 2009)
795 was used in 'mem' mode on viral RNASeq reads. After generating this alignment using
796 the default parameters and same reference SARS-CoV-2 FASTA file as above, chimeric
797 reads were isolated by searching for all reads containing the 'SA' tag and the SARS TRS
798 sequence, 'AAACGAAC'. SARS-CoV-2 gRNAs were extracted by searching for all reads
799 containing the first 15-20 bases of the ORF1A coding sequence (CDS), as these
800 sequences would only be present in full-length SARS-CoV-2 genomes. This provided the
801 sequences and alignment locations of the chimeric and genomic reads, which were then

802 visualized using R. For sgRNAs, the viral gene corresponding to each transcript was
803 determined by locating the CDS with the nearest downstream start site. This data,
804 together with the number of gRNAs was used to calculate relative percentages of viral
805 transcripts and, together with the total number of mapped viral reads, allowed for the
806 tabulation of viral gene counts at each time point. For ribosome profiling data,
807 featureCounts was used to enumerate the number of viral reads, as ribosomes only
808 translate the first gene on each transcript and so footprints from nested 3' gene were low
809 enough to be negligible.
810
811 **SUPPLEMENTARY FIGURE LEGENDS**
812 **Figure S1. SARS-CoV-2 infection of Vero E6 cells (Supplemental to Figure 1 and**
813 **Figure 2).** Vero cells were infected at an MOI of 0.1 pfu/cell (A) or 2 pfu/cell (B). Infected
814 cells were fixed at the indicated time points post-infection and stained using an antibody
815 against the viral N protein and visualized by microscopy.\
816
817 **Figure S2. Quality control of Ribo-seq libraries derived from Vero E6 cells infected**
818 **with SARS-CoV-2 at a low MOI (Supplemental to Figure 1).** Vero E6 cells infected as
819 in Fig. 1A at an MOI of 0.1 pfu/cell were processed for ribo-seq as detailed in Materials
820 and Methods. (A) Length distribution of ribo-seq-derived reads mapping to the African
821 green monkey (AGM) transcriptome are shown from independent replicates. (B) Length
822 distribution of ribo-seq-derived reads mapping to SARS-CoV-2 genome. (C) Number or
823 reads mapping to 5'UTR, CDS and 3' UTRs of annotated AGM genes in matching RNA-
824 seq and ribo-seq libraries are shown. (D) Meta-profiles showing the periodicity of
825 ribosomes along the AGM transcripts at the genome-wide scale from independent
826 replicate samples. (E, F) Length distribution of ribo-seq-derived reads mapping to anti-
827 sense SARS-CoV-2 transcripts (E) or SARS-CoV-2 ORF1ab region (F).

828

829 **Figure S3. Length distribution of ribo-seq reads derived from Vero E6 cells infected**
830 **with SARS-CoV-2 at a high MOI (Supplemental to Figure 2).** Vero E6 cells infected
831 with SARS-CoV-2 as in Fig. 1A at an MOI of 2 pfu/cell were processed for ribo-seq as
832 detailed in Materials and Methods. (A) Length distribution of ribo-seq-derived reads
833 mapping to the African green monkey (AGM) transcriptome are shown from independent
834 replicates. (B, C) Length distribution of ribo-seq-derived reads mapping to SARS-CoV-2
835 genome (B) or anti-sense SARS-CoV-2 transcripts (C) from independent experiments are
836 shown.

837

838 **Figure S4. Ribo-seq-derived reads map to 5'UTRs and CDSs but are depleted of**
839 **3'UTRs (Supplemental to Figure 2).** Vero E6 cells infected with SARS-CoV-2 as in Fig.
840 1A at an MOI of 2 pfu/cell were processed for ribo-seq and RNA-seq as detailed in
841 Materials and Methods. Reads mapping to 5'UTRs, CDSs and 3'UTRs of the AGM
842 transcriptome are depicted for the indicated samples.

843

844 **Figure S5. Metaprofiles and P-site analyses of ribo-seq reads derived from Vero E6**
845 **cells infected at a MOI of 2 pfu/cell (Supplemental to Figure 2).** Meta-profiles showing
846 the periodicity of ribosomes along the AGM transcripts at the genome-wide scale from
847 independent ribo-seq libraries.

848

849 **Figure S6. RNA-seq on sense and antisense SARS-CoV-2 transcripts during low**
850 **MOI infection (Supplemental to Figure 1).** Data derived from experiments described in
851 Figure 1 and a replicate experiment were plotted to demonstrate the number of reads that
852 map to sense vs. antisense transcripts at 24 (A) and 48 (B) hpi. Schematic diagram of
853 SARS-CoV-2 genome features shown below is co-linear.

854

855 **Figure S7. Ribosome occupancy on the SARS-CoV-2 genome during low MOI**
856 **infection (Supplemental to Figure 1).** Vero E6 cells were infected at 0.1 pfu/cell and
857 cells were processed for RNA-seq and Ribo-seq as in Figure 1. Ribo-seq and RNA-seq
858 reads (counts) mapping to the first 20000 nucleotides (ORF1ab) of the viral genome at 24
859 (A) and 48 (B) hpi with constituent non-structural proteins (NSPs) shown below is co-
860 linear.

861

862 **Figure S8. Ribosome occupancy on sense and antisense SARS-CoV-2 transcripts**
863 **during low MOI infection (Supplemental to Figure 1).** Ribo-seq data derived from the
864 two independent experiments described in Figure 1 were plotted to demonstrate the
865 number of reads mapping to sense and antisense transcripts at 24 (A, C) and 48 (B, D)
866 hpi. Schematic diagram of SARS2 genome features shown below is co-linear.

867

868 **Figure S9. RNA-seq on sense and antisense SARS-CoV-2 transcripts during high**
869 **MOI infection (Supplemental to Figure 2).** RNA-seq data derived from experiments
870 described in Figure 1 were plotted to demonstrate the number of reads that map to
871 sense and. antisense transcripts at 2 hpi (A), 6 hpi (B), 12 hpi (C), 24 hpi (D) and 48 hpi
872 (E). Schematic diagram of SARS2 genome features shown below is co-linear.

873
874 **Figure S10. Reproducibility of RNA-seq experiments (Supplemental to Figure 2).**
875 RNA-seq data derived from a replicate experiment described in Figure 1 were plotted to
876 demonstrate the number of reads that map to sense vs. antisense transcripts at 2 hpi (A),
877 6 hpi (B), 12 hpi (C), 24 hpi (D) and 48 hpi (E). Schematic diagram of SARS2 genome
878 features shown below is co-linear.

879

880 **Figure S11. Ribosome occupancy on sense and antisense SARS-CoV-2 transcripts**
881 **during high MOI infection (Supplemental to Figure 2).** Ribo-seq data derived from
882 experiments described in Figure 1 were plotted to demonstrate the number of reads that
883 map to sense vs. antisense transcripts at 2 hpi (A), 6 hpi (B), 12 hpi (C), 24 hpi (D) and 48
884 hpi (E). Schematic diagram of SARS2 genome features shown below is co-linear.
885
886 **Figure S12. Reproducibility of Ribo-seq experiments (Supplemental to Figure 2).**
887 Ribo-seq data derived from a replicate experiment described in Figure 1 were plotted to
888 demonstrate the number of reads that map to sense vs. antisense transcripts at 2 hpi (A),
889 6 hpi (B), 12 hpi (C), 24 hpi (D) and 48 hpi (E). Schematic diagram of SARS2 genome
890 features shown below is co-linear.
891
892 **Figure S13. Properties of the high ribosome occupancy site located between 27371-**
893 **27457 nt (supplemental to Figure 2).** (A) Sequence homology of the high ribosome
894 occupancy site between SARS-CoV-2 27371-27457nts and SARS-CoV (27243-27336).
895 (B) Predicted secondary structure of the SARS-CoV-2 sequence at 27371-27457nts using
896 RNAstructure. (C) Ribosome occupancy surrounding nucleotides 27371-27457 at the
897 indicated time points post-infection.
898
899 **Figure S14. Ribosome occupancy remains low within the SARS-CoV-2 frameshifting**
900 **site throughout infection (supplemental to Figure 2).** (A-E) Ribosome occupancy
901 surrounding and within the frameshifting site at the indicated time points post-infection
902 (derived from Ribo-seq experiments in Figure 2) is shown. Red bars indicate the position
903 of the frameshifting element. (F) Length distribution of ribo-seq-derived reads mapping to
904 SARS-CoV-2 ORF1ab. (G) ORF1arameshifting efficiency of SARS-CoV-2 throughout the
905 course of infection.

906

907 **Figure S15. Quality control of Ribo-seq libraries derived from primary CD4+ T-cells**
908 **infected with HIV-1 (Supplemental to Figure 2).** CD4+ T-cells isolated from two
909 independent donors infected HIV-1 were processed for ribo-seq as detailed in Materials
910 and Methods. Length distribution of ribo-seq-derived reads mapping to the human
911 transcriptome (A) and HIV-1 genome (B) are shown for independent replicates. (C) Meta-
912 profiles showing the periodicity of ribosomes along the human transcripts at the genome-
913 wide scale from independent replicate samples. (D) Number or reads mapping to 5'UTR,
914 CDS and 3' UTRs of annotated human genes in matching RNA-seq and ribo-seq libraries
915 are shown.

916

917 **Figure S16. RIbo-seq in HIV-1-infected cells reveals structural elements that**
918 **regulate translation (supplemental to Figure 2).** Primary CD4+ T-cells were infected
919 with HIV-1_{NL4-3}/VSV-G at an MOI of 2 and infected cells processed for RNA-seq and Ribo-
920 seq at 24 hpi. (A) Ribo-seq and RNA-seq reads (counts) mapping to the HIV-1 genome is
921 shown. Schematic diagram of HIV-1 genome features shown below is co-linear. (B)
922 Secondary structure prediction of the HIV-1 ribosome frameshifting element is shown. (C)
923 Ribosome occupancy within the frameshifting site is shown.

924

925 **Figure S17. SARS-CoV-2 infection of primary HBECs grown at ALI (supplemental to**
926 **Figure 3).** (A) Primary HBEC cultures were infected with SARS-CoV-2 at an MOI of 0.5
927 pfu/cell and fixed at 72 hpi. Cells were probed with anti-spike (anti-S) and anti-
928 nucleoprotein (anti-N) antibodies and imaged by microscopy. (B, C) Primary HBEC
929 cultures were infected with SARS-CoV-2 at an MOI of 1 pfu/cell and fixed at 96 hpi. Cells
930 were probed with RNAScope probes against sense- and anti-sense SARS-CoV-2
931 transcripts, and imaged by microscopy with a 4X (B) or 20X objective (C). (D) Primary

932 HBEC cultures were infected with SARS-CoV-2-NeonGreen and imaged live during the
933 course of infection at the indicated time points.
934
935 **Figure S18. Quality of ribo-seq experiments from SARS-CoV-2-infected primary**
936 **HBECs grown at ALI (supplemental to Figure 3).** Primary HBEC cultures were infected
937 with SARS-CoV-2 at an MOI of 0.5 or MOI of 1 pfu/cell as in Figure 3 and processed for
938 ribo-seq at the indicated times post-infection. (A, B) Length distribution of ribo-seq-derived
939 reads mapping to the human transcriptome (A) and SARS-CoV-2 genome (B) are shown.
940 (C) Number or reads mapping to 5'UTR, CDS and 3' UTRs of annotated human genes in
941 matching RNA-seq and ribo-seq libraries are shown.
942 **Figure S19. Metaprofiles and P-site analyses of ribo-seq reads derived from SARS-**
943 **CoV-2-infected primary HBEC cells (Supplemental to Figure 3).** Meta-profiles
944 showing the periodicity of ribosomes along the human transcripts at the genome-wide
945 scale from independent ribo-seq libraries derived from primary HBECs infected at the
946 indicated MOIs and times post-infection.
947
948 **Figure S20. Reproducibility of RNA-seq and ribo-seq data sets (supplemental to**
949 **Figure 4). (A)** Correlation of $\log_2$(counts per million mapped reads) for each gene
950 derived from RNA-seq experiments is shown. **(B)** Correlation of $\log_2$ counts per million
951 mapped reads for each gene derived from ribo-seq experiments is shown.
952
953 **Figure S21. Time-course analysis of differentially expressed genes in response to**
954 **SARS-CoV-2 infection (Supplemental to Figure 4**). Differentially expressed genes
955 across different time points from Figure 4 were plotted to demonstrate the time-course
956 progression of differential gene expression in RNA-seq and ribo-seq data sets. Data

957 show the log_2(fold-change) values of genes that are up- or down-regulated greater than
958 2-fold with FDR<0.05.
959
960 **Figure S22. Time-course analysis of differentially expressed genes in response to**
961 **SARS-CoV-2 infection (Supplemental to Figure 4**). Log_2(cpm) values of differentially
962 expressed genes from Figure 4 are plotted for each experiment.
963
964 **Figure S23. SARS-CoV-2 infection induces a general decrease in host mRNA**
965 **expression (high MOI, supplemental to Figure 4).** Vero E6 cells were infected at 2
966 pfu/cell and cells were processed for RNA-seq. Volcano plots show the log_2 fold-change
967 (x-axis) vs. significance (-log(Pvalue), y-axis) of host genes at 2 hpi (A), 6 hpi (B), 12 hpi
968 (C), 24 hpi (D) and 48 hpi (E). Top differentially expressed genes (FDR<0.05, fold
969 change>2) are indicated by blue dots.
970
971 **Figure S24. SARS-CoV-2 infection results in lower translation rates for mRNAs**
972 **coding for immune responses (supplemental to Figure 4).** Expression levels (fold
973 change over mock) of select immune-related mRNAs that were significantly upregulated
974 in RNA-seq data set were compared to expression levels derived from ribo-seq data set.
975
976 **Figure S25. Differentially transcribed and translated host genes in SARS-CoV-2-**
977 **infected cells (supplemental to Figure 4).** Vero E6 cells were infected at 2 pfu/cell and
978 processed for RNA-seq at 2 hpi and Ribo-seq at 24 hpi (A, C) and 48 hpi (B, D).
979 Heatmaps show the log_2 counts per million mapped reads (cpm) of the top differentially
980 expressed genes (FDR<0.05, fold change>2) derived from two independent
981 experiments. Scale of each graph is shown below.
982

983 **Figure S26. Reproducibility of RNA-seq and ribo-seq data sets (supplemental to**
984 **Figure 7). (A)** Correlation of $\log_2$(counts per million mapped reads) for each gene
985 derived from RNA-seq experiments (low MOI) is shown. **(B)** Correlation of $\log_2$ counts
986 per million mapped reads for each gene derived from ribo-seq experiments (low MOI) is
987 shown.
988
989 **Figure S27. Transcriptional responses of HBECs to SARS-CoV-2.** HBECs grown at
990 ALI were infected with SARS-CoV-2 at a MOI of 0.5 i.u./cell and processed for RNA-seq
991 (A) and ribo-seq (B) at 6, 24 and 48 hpi. Data were analyzed for trends in gene set
992 enrichment over the period of infection.
993
994 **REFERENCES**

995 BARIL, M., DULUDE, D., GENDRON, K., LEMAY, G. & BRAKIER-GINGRAS, L. 2003.
996 Efficiency of a programmed -1 ribosomal frameshift in the different subtypes
997 of the human immunodeficiency virus type 1 group M. *RNA,* 9**,** 1246-53.
998 BEAUPARLANT, C. J., LAMAZE, F.C., SAMB, R., LIPPENS, C., DESCHENES, A.L., DROIT,
999 A. 2020. metagene: A package to produce metagene plots. R package version
1000 2.20.0. .
1001 BETTUM, I. J., VASILIAUSKAITE, K., NYGAARD, V., CLANCY, T., PETTERSEN, S. J.,
1002 TENSTAD, E., MAELANDSMO, G. M. & PRASMICKAITE, L. 2014. Metastasis-
1003 associated protein S100A4 induces a network of inflammatory cytokines that
1004 activate stromal cells to acquire pro-tumorigenic properties. *Cancer Lett,* 344**,**
1005 28-39.
1006 BHARADWAJ, A., BYDOUN, M., HOLLOWAY, R. & WAISMAN, D. 2013. Annexin A2
1007 heterotetramer: structure and function. *Int J Mol Sci,* 14**,** 6259-305.
1008 BIDOU, L., STAHL, G., GRIMA, B., LIU, H., CASSAN, M. & ROUSSET, J. P. 1997. In vivo
1009 HIV-1 frameshifting efficiency is directly related to the stability of the stem-
1010 loop stimulatory signal. *RNA,* 3**,** 1153-8.
1011 BISWAS, P., JIANG, X., PACCHIA, A. L., DOUGHERTY, J. P. & PELTZ, S. W. 2004. The
1012 human immunodeficiency virus type 1 ribosomal frameshifting site is an
1013 invariant sequence determinant and an important target for antiviral therapy.
1014 *J Virol,* 78**,** 2082-7.
1015 BLANCO-MELO, D., NILSSON-PAYANT, B. E., LIU, W. C., UHL, S., HOAGLAND, D.,
1016 MOLLER, R., JORDAN, T. X., OISHI, K., PANIS, M., SACHS, D., WANG, T. T.,
1017 SCHWARTZ, R. E., LIM, J. K., ALBRECHT, R. A. & TENOEVER, B. R. 2020.

1018 Imbalanced Host Response to SARS-CoV-2 Drives Development of COVID-19.
1019 *Cell,* 181**,** 1036-1045 e9.
1020 BRIERLEY, I. & DOS RAMOS, F. J. 2006. Programmed ribosomal frameshifting in HIV-
1021 1 and the SARS-CoV. *Virus Res,* 119**,** 29-42.
1022 BUTLER, D. J., MOZSARY, C., MEYDAN, C., DANKO, D., FOOX, J., ROSIENE, J., SHAIBER,
1023 A., AFSHINNEKOO, E., MACKAY, M., SEDLAZECK, F. J., IVANOV, N. A., SIERRA,
1024 M., POHLE, D., ZIETZ, M., GISLADOTTIR, U., RAMLALL, V., WESTOVER, C. D.,
1025 RYON, K., YOUNG, B., BHATTACHARYA, C., RUGGIERO, P., LANGHORST, B. W.,
1026 TANNER, N., GAWRYS, J., MELESHKO, D., XU, D., STEEL, P. A. D., SHEMESH, A.
1027 J., XIANG, J., THIERRY-MIEG, J., THIERRY-MIEG, D., SCHWARTZ, R. E., IFTNER,
1028 A., BEZDAN, D., SIPLEY, J., CONG, L., CRANEY, A., VELU, P., MELNICK, A. M.,
1029 HAJIRASOULIHA, I., HORNER, S. M., IFTNER, T., SALVATORE, M., LODA, M.,
1030 WESTBLADE, L. F., CUSHING, M., LEVY, S., WU, S., TATONETTI, N., IMIELINSKI,
1031 M., RENNERT, H. & MASON, C. E. 2020. Shotgun Transcriptome and Isothermal
1032 Profiling of SARS-CoV-2 Infection Reveals Unique Host Responses, Viral
1033 Diversification, and Drug Interactions. *bioRxiv*.
1034 CHANG, S. Y., SUTTHENT, R., AUEWARAKUL, P., APICHARTPIYAKUL, C., ESSEX, M. &
1035 LEE, T. H. 1999. Differential stability of the mRNA secondary structures in the
1036 frameshift site of various HIV type 1 viruses. *AIDS Res Hum Retroviruses,* 15**,**
1037 1591-6.
1038 CHANNAPPANAVAR, R. & PERLMAN, S. 2017. Pathogenic human coronavirus
1039 infections: causes and consequences of cytokine storm and immunopathology.
1040 *Semin Immunopathol,* 39**,** 529-539.
1041 CHEN, G., CHANG, K. Y., CHOU, M. Y., BUSTAMANTE, C. & TINOCO, I., JR. 2009. Triplex
1042 structures in an RNA pseudoknot enhance mechanical stability and increase
1043 efficiency of -1 ribosomal frameshifting. *Proc Natl Acad Sci U S A,* 106**,** 12706-
1044 11.
1045 DAFFIS, S., SZRETTER, K. J., SCHRIEWER, J., LI, J., YOUN, S., ERRETT, J., LIN, T. Y.,
1046 SCHNELLER, S., ZUST, R., DONG, H., THIEL, V., SEN, G. C., FENSTERL, V.,
1047 KLIMSTRA, W. B., PIERSON, T. C., BULLER, R. M., GALE, M., JR., SHI, P. Y. &
1048 DIAMOND, M. S. 2010. 2'-O methylation of the viral mRNA cap evades host
1049 restriction by IFIT family members. *Nature,* 468**,** 452-6.
1050 DE WIT, E., VAN DOREMALEN, N., FALZARANO, D. & MUNSTER, V. J. 2016. SARS and
1051 MERS: recent insights into emerging coronaviruses. *Nat Rev Microbiol,* 14**,**
1052 523-34.
1053 DIAMOND, M. S. & FARZAN, M. 2013. The broad-spectrum antiviral functions of IFIT
1054 and IFITM proteins. *Nat Rev Immunol,* 13**,** 46-57.
1055 DINAN, A. M., KEEP, S., BICKERTON, E., BRITTON, P., FIRTH, A. E. & BRIERLEY, I. 2019.
1056 Comparative Analysis of Gene Expression in Virulent and Attenuated Strains
1057 of Infectious Bronchitis Virus at Subcodon Resolution. *J Virol,* 93.
1058 DINMAN, J. D. 2012. Mechanisms and implications of programmed translational
1059 frameshifting. *Wiley Interdiscip Rev RNA,* 3**,** 661-73.
1060 DOBIN, A., DAVIS, C. A., SCHLESINGER, F., DRENKOW, J., ZALESKI, C., JHA, S., BATUT,
1061 P., CHAISSON, M. & GINGERAS, T. R. 2013. STAR: ultrafast universal RNA-seq
1062 aligner. *Bioinformatics,* 29**,** 15-21.

1063 DULUDE, D., BERCHICHE, Y. A., GENDRON, K., BRAKIER-GINGRAS, L. & HEVEKER, N.
1064 2006. Decreasing the frameshift efficiency translates into an equivalent
1065 reduction of the replication of the human immunodeficiency virus type 1.
1066 *Virology,* 345**,** 127-36.
1067 FARABAUGH, P. J. 1996. Programmed translational frameshifting. *Microbiol Rev,* 60**,**
1068 103-34.
1069 FENSTERL, V. & SEN, G. C. 2015. Interferon-induced Ifit proteins: their role in viral
1070 pathogenesis. *J Virol,* 89**,** 2462-8.
1071 FINKEL, Y., MIZRAHI, O., NACHSHON, A., WEINGARTEN-GABBAY, S., MORGENSTERN,
1072 D., YAHALOM-RONEN, Y., TAMIR, H., ACHDOUT, H., STEIN, D., ISRAELI, O.,
1073 BETH-DIN, A., MELAMED, S., WEISS, S., ISRAELY, T., PARAN, N., SCHWARTZ, M.
1074 & STERN-GINOSSAR, N. 2020. The coding capacity of SARS-CoV-2. *Nature*.
1075 GARCIA-MIRANDA, P., BECKER, J. T., BENNER, B. E., BLUME, A., SHERER, N. M. &
1076 BUTCHER, S. E. 2016. Stability of HIV Frameshift Site RNA Correlates with
1077 Frameshift Efficiency and Decreased Virus Infectivity. *J Virol,* 90**,** 6906-6917.
1078 GIEDROC, D. P. & CORNISH, P. V. 2009. Frameshifting RNA pseudoknots: structure
1079 and mechanism. *Virus Res,* 139**,** 193-208.
1080 HANSEN, T. M., REIHANI, S. N., ODDERSHEDE, L. B. & SORENSEN, M. A. 2007.
1081 Correlation between mechanical strength of messenger RNA pseudoknots and
1082 ribosomal frameshifting. *Proc Natl Acad Sci U S A,* 104**,** 5830-5.
1083 HEJBLUM, B. P., SKINNER, J. & THIEBAUT, R. 2015. Time-Course Gene Set Analysis for
1084 Longitudinal Gene Expression Data. *PLoS Comput Biol,* 11**,** e1004310.
1085 HORANI, A., DRULEY, T. E., ZARIWALA, M. A., PATEL, A. C., LEVINSON, B. T., VAN
1086 ARENDONK, L. G., THORNTON, K. C., GIACALONE, J. C., ALBEE, A. J., WILSON, K.
1087 S., TURNER, E. H., NICKERSON, D. A., SHENDURE, J., BAYLY, P. V., LEIGH, M. W.,
1088 KNOWLES, M. R., BRODY, S. L., DUTCHER, S. K. & FERKOL, T. W. 2012. Whole-
1089 exome capture and sequencing identifies HEATR2 mutation as a cause of
1090 primary ciliary dyskinesia. *Am J Hum Genet,* 91**,** 685-93.
1091 HORANI, A., USTIONE, A., HUANG, T., FIRTH, A. L., PAN, J., GUNSTEN, S. P., HASPEL, J.
1092 A., PISTON, D. W. & BRODY, S. L. 2018. Establishment of the early cilia
1093 preassembly protein complex during motile ciliogenesis. *Proc Natl Acad Sci U*
1094 *S A,* 115**,** E1221-E1228.
1095 HUANG, C., LOKUGAMAGE, K. G., ROZOVICS, J. M., NARAYANAN, K., SEMLER, B. L. &
1096 MAKINO, S. 2011. SARS coronavirus nsp1 protein induces template-
1097 dependent endonucleolytic cleavage of mRNAs: viral mRNAs are resistant to
1098 nsp1-induced RNA cleavage. *PLoS Pathog,* 7**,** e1002433.
1099 HUANG, J., HUME, A. J., ABO, K. M., WERDER, R. B., VILLACORTA-MARTIN, C.,
1100 ALYSANDRATOS, K. D., BEERMANN, M. L., SIMONE-ROACH, C., OLEJNIK, J.,
1101 SUDER, E. L., BULLITT, E., HINDS, A., SHARMA, A., BOSMANN, M., WANG, R.,
1102 HAWKINS, F., BURKS, E. J., SAEED, M., WILSON, A. A., MUHLBERGER, E. &
1103 KOTTON, D. N. 2020. SARS-CoV-2 Infection of Pluripotent Stem Cell-derived
1104 Human Lung Alveolar Type 2 Cells Elicits a Rapid Epithelial-Intrinsic
1105 Inflammatory Response. *bioRxiv*.
1106 HUANG, X., YANG, Y., WANG, G., CHENG, Q. & DU, Z. 2014. Highly conserved RNA
1107 pseudoknots at the Gag-Pol junction of HIV-1 suggest a novel mechanism of -1
1108 ribosomal frameshifting. *RNA,* 20**,** 587-93.

1109 HYDE, J. L. & DIAMOND, M. S. 2015. Innate immune restriction and antagonism of viral
1110 RNA lacking 2-O methylation. *Virology,* 479-480**,** 66-74.
1111 INGOLIA, N. T., BRAR, G. A., ROUSKIN, S., MCGEACHY, A. M. & WEISSMAN, J. S. 2012.
1112 The ribosome profiling strategy for monitoring translation in vivo by deep
1113 sequencing of ribosome-protected mRNA fragments. *Nat Protoc,* 7**,** 1534-50.
1114 INGOLIA, N. T., GHAEMMAGHAMI, S., NEWMAN, J. R. & WEISSMAN, J. S. 2009.
1115 Genome-wide analysis in vivo of translation with nucleotide resolution using
1116 ribosome profiling. *Science,* 324**,** 218-23.
1117 IRIGOYEN, N., FIRTH, A. E., JONES, J. D., CHUNG, B. Y., SIDDELL, S. G. & BRIERLEY, I.
1118 2016. High-Resolution Analysis of Coronavirus Gene Expression by RNA
1119 Sequencing and Ribosome Profiling. *PLoS Pathog,* 12**,** e1005473.
1120 JACKS, T., POWER, M. D., MASIARZ, F. R., LUCIW, P. A., BARR, P. J. & VARMUS, H. E.
1121 1988. Characterization of ribosomal frameshifting in HIV-1 gag-pol
1122 expression. *Nature,* 331**,** 280-3.
1123 JAFARZADEH, A., CHAUHAN, P., SAHA, B., JAFARZADEH, S. & NEMATI, M. 2020.
1124 Contribution of monocytes and macrophages to the local tissue inflammation
1125 and cytokine storm in COVID-19: Lessons from SARS and MERS, and potential
1126 therapeutic interventions. *Life Sci***,** 118102.
1127 JAMES, C. C. & SMYTH, J. W. 2018. Alternative mechanisms of translation initiation:
1128 An emerging dynamic regulator of the proteome in health and disease. *Life Sci,*
1129 212**,** 138-144.
1130 KAMITANI, W., HUANG, C., NARAYANAN, K., LOKUGAMAGE, K. G. & MAKINO, S. 2009.
1131 A two-pronged strategy to suppress host protein synthesis by SARS
1132 coronavirus Nsp1 protein. *Nat Struct Mol Biol,* 16**,** 1134-40.
1133 KIM, D., LEE, J. Y., YANG, J. S., KIM, J. W., KIM, V. N. & CHANG, H. 2020. The Architecture
1134 of SARS-CoV-2 Transcriptome. *Cell,* 181**,** 914-921 e10.
1135 KOPECKY-BROMBERG, S. A., MARTINEZ-SOBRIDO, L. & PALESE, P. 2006. 7a protein
1136 of severe acute respiratory syndrome coronavirus inhibits cellular protein
1137 synthesis and activates p38 mitogen-activated protein kinase. *J Virol,* 80**,** 785-
1138 93.
1139 KORNIY, N., SAMATOVA, E., ANOKHINA, M. M., PESKE, F. & RODNINA, M. V. 2019.
1140 Mechanisms and biomedical implications of -1 programmed ribosome
1141 frameshifting on viral and bacterial mRNAs. *FEBS Lett,* 593**,** 1468-1482.
1142 KUTLUAY, S. B. & BIENIASZ, P. D. 2016. Analysis of HIV-1 Gag-RNA Interactions in
1143 Cells and Virions by CLIP-seq. *Methods Mol Biol,* 1354**,** 119-31.
1144 KUTLUAY, S. B., ZANG, T., BLANCO-MELO, D., POWELL, C., JANNAIN, D., ERRANDO, M.
1145 & BIENIASZ, P. D. 2014. Global changes in the RNA binding specificity of HIV-
1146 1 gag regulate virion genesis. *Cell,* 159**,** 1096-1109.
1147 KWAN, T. & THOMPSON, S. R. 2019. Noncanonical Translation Initiation in
1148 Eukaryotes. *Cold Spring Harb Perspect Biol,* 11.
1149 LANGMEAD, B., TRAPNELL, C., POP, M. & SALZBERG, S. L. 2009. Ultrafast and
1150 memory-efficient alignment of short DNA sequences to the human genome.
1151 *Genome Biol,* 10**,** R25.
1152 LAURIA, F., TEBALDI, T., BERNABO, P., GROEN, E. J. N., GILLINGWATER, T. H. & VIERO,
1153 G. 2018. riboWaltz: Optimization of ribosome P-site positioning in ribosome
1154 profiling data. *PLoS Comput Biol,* 14**,** e1006169.

1155 LI, H. & DURBIN, R. 2009. Fast and accurate short read alignment with Burrows-
1156 Wheeler transform. *Bioinformatics,* 25**,** 1754-60.
1157 LI, H., HANDSAKER, B., WYSOKER, A., FENNELL, T., RUAN, J., HOMER, N., MARTH, G.,
1158 ABECASIS, G., DURBIN, R. & GENOME PROJECT DATA PROCESSING, S. 2009.
1159 The Sequence Alignment/Map format and SAMtools. *Bioinformatics,* 25**,** 2078-
1160 9.
1161 LI, M. M., MACDONALD, M. R. & RICE, C. M. 2015. To translate, or not to translate: viral
1162 and host mRNA regulation by interferon-stimulated genes. *Trends Cell Biol,* 25**,**
1163 320-9.
1164 LI, Z., LI, Y., LIU, S. & QIN, Z. 2020. Extracellular S100A4 as a key player in fibrotic
1165 diseases. *J Cell Mol Med,* 24**,** 5973-5983.
1166 LIU, Y., MYRVANG, H. K. & DEKKER, L. V. 2015. Annexin A2 complexes with S100
1167 proteins: structure, function and pharmacological manipulation. *Br J*
1168 *Pharmacol,* 172**,** 1664-76.
1169 LOKUGAMAGE, K. G., NARAYANAN, K., HUANG, C. & MAKINO, S. 2012. Severe acute
1170 respiratory syndrome coronavirus protein nsp1 is a novel eukaryotic
1171 translation inhibitor that represses multiple steps of translation initiation. *J*
1172 *Virol,* 86**,** 13598-608.
1173 MASTERS, P. S. 2006. The molecular biology of coronaviruses. *Adv Virus Res,* 66**,** 193-
1174 292.
1175 MENACHERY, V. D., EISFELD, A. J., SCHAFER, A., JOSSET, L., SIMS, A. C., PROLL, S., FAN,
1176 S., LI, C., NEUMANN, G., TILTON, S. C., CHANG, J., GRALINSKI, L. E., LONG, C.,
1177 GREEN, R., WILLIAMS, C. M., WEISS, J., MATZKE, M. M., WEBB-ROBERTSON, B.
1178 J., SCHEPMOES, A. A., SHUKLA, A. K., METZ, T. O., SMITH, R. D., WATERS, K. M.,
1179 KATZE, M. G., KAWAOKA, Y. & BARIC, R. S. 2014. Pathogenic influenza viruses
1180 and coronaviruses utilize similar and contrasting approaches to control
1181 interferon-stimulated gene responses. *mBio,* 5**,** e01174-14.
1182 MITCHELL, H. D., EISFELD, A. J., SIMS, A. C., MCDERMOTT, J. E., MATZKE, M. M., WEBB-
1183 ROBERTSON, B. J., TILTON, S. C., TCHITCHEK, N., JOSSET, L., LI, C., ELLIS, A. L.,
1184 CHANG, J. H., HEEGEL, R. A., LUNA, M. L., SCHEPMOES, A. A., SHUKLA, A. K.,
1185 METZ, T. O., NEUMANN, G., BENECKE, A. G., SMITH, R. D., BARIC, R. S.,
1186 KAWAOKA, Y., KATZE, M. G. & WATERS, K. M. 2013. A network integration
1187 approach to predict conserved regulators related to pathogenicity of influenza
1188 and SARS-CoV respiratory viruses. *PLoS One,* 8**,** e69374.
1189 MOOTHA, V. K., LINDGREN, C. M., ERIKSSON, K. F., SUBRAMANIAN, A., SIHAG, S.,
1190 LEHAR, J., PUIGSERVER, P., CARLSSON, E., RIDDERSTRALE, M., LAURILA, E.,
1191 HOUSTIS, N., DALY, M. J., PATTERSON, N., MESIROV, J. P., GOLUB, T. R.,
1192 TAMAYO, P., SPIEGELMAN, B., LANDER, E. S., HIRSCHHORN, J. N., ALTSHULER,
1193 D. & GROOP, L. C. 2003. PGC-1alpha-responsive genes involved in oxidative
1194 phosphorylation are coordinately downregulated in human diabetes. *Nat*
1195 *Genet,* 34**,** 267-73.
1196 MOUZAKIS, K. D., LANG, A. L., VANDER MEULEN, K. A., EASTERDAY, P. D. & BUTCHER,
1197 S. E. 2013. HIV-1 frameshift efficiency is primarily determined by the stability
1198 of base pairs positioned at the mRNA entrance channel of the ribosome.
1199 *Nucleic Acids Res,* 41**,** 1901-13.

1200 NAKAGAWA, K., LOKUGAMAGE, K. G. & MAKINO, S. 2016. Viral and Cellular mRNA
1201 Translation in Coronavirus-Infected Cells. *Adv Virus Res,* 96**,** 165-192.
1202 NARAYANAN, K., HUANG, C., LOKUGAMAGE, K., KAMITANI, W., IKEGAMI, T., TSENG,
1203 C. T. & MAKINO, S. 2008. Severe acute respiratory syndrome coronavirus nsp1
1204 suppresses host gene expression, including that of type I interferon, in infected
1205 cells. *J Virol,* 82**,** 4471-9.
1206 NARAYANAN, K., RAMIREZ, S. I., LOKUGAMAGE, K. G. & MAKINO, S. 2015. Coronavirus
1207 nonstructural protein 1: Common and distinct functions in the regulation of
1208 host and viral gene expression. *Virus Res,* 202**,** 89-100.
1209 PARKIN, N. T., CHAMORRO, M. & VARMUS, H. E. 1992. Human immunodeficiency virus
1210 type 1 gag-pol frameshifting is dependent on downstream mRNA secondary
1211 structure: demonstration by expression in vivo. *J Virol,* 66**,** 5147-51.
1212 PERLMAN, S. & DANDEKAR, A. A. 2005. Immunopathogenesis of coronavirus
1213 infections: implications for SARS. *Nat Rev Immunol,* 5**,** 917-27.
1214 PLANT, E. P. & DINMAN, J. D. 2008. The role of programmed-1 ribosomal
1215 frameshifting in coronavirus propagation. *Front Biosci,* 13**,** 4873-81.
1216 PLANT, E. P., JACOBS, K. L., HARGER, J. W., MESKAUSKAS, A., JACOBS, J. L., BAXTER, J.
1217 L., PETROV, A. N. & DINMAN, J. D. 2003. The 9-A solution: how mRNA
1218 pseudoknots promote efficient programmed -1 ribosomal frameshifting. *RNA,*
1219 9**,** 168-74.
1220 RAO, S., HOSKINS, I., GARCIA, P. D., TONN, T., OZADAM, H., CENIK, E. S. & CENIK, C.
1221 2020. Genes with 5' terminal oligopyrimidine tracts preferentially escape
1222 global suppression of translation by the SARS-CoV-2 NSP1 protein. *bioRxiv*.
1223 REYNAUD, J. M., KIM, D. Y., ATASHEVA, S., RASALOUSKAYA, A., WHITE, J. P.,
1224 DIAMOND, M. S., WEAVER, S. C., FROLOVA, E. I. & FROLOV, I. 2015. IFIT1
1225 Differentially Interferes with Translation and Replication of Alphavirus
1226 Genomes and Promotes Induction of Type I Interferon. *PLoS Pathog,* 11**,**
1227 e1004863.
1228 RIBA, A., DI NANNI, N., MITTAL, N., ARHNE, E., SCHMIDT, A. & ZAVOLAN, M. 2019.
1229 Protein synthesis rates and ribosome occupancies reveal determinants of
1230 translation elongation rates. *Proc Natl Acad Sci U S A,* 116**,** 15023-15032.
1231 ROBINSON, M. D., MCCARTHY, D. J. & SMYTH, G. K. 2010. edgeR: a Bioconductor
1232 package for differential expression analysis of digital gene expression data.
1233 *Bioinformatics,* 26**,** 139-40.
1234 SCHUBERT, K., KAROUSIS, E. D., JOMAA, A., SCAIOLA, A., ECHEVERRIA, B., GURZELER,
1235 L. A., LEIBUNDGUT, M., THIEL, V., MUHLEMANN, O. & BAN, N. 2020. SARS-CoV-
1236 2 Nsp1 binds the ribosomal mRNA channel to inhibit translation. *Nat Struct*
1237 *Mol Biol,* 27**,** 959-966.
1238 SHEHU-XHILAGA, M., CROWE, S. M. & MAK, J. 2001. Maintenance of the Gag/Gag-Pol
1239 ratio is important for human immunodeficiency virus type 1 RNA dimerization
1240 and viral infectivity. *J Virol,* 75**,** 1834-41.
1241 STAPLE, D. W. & BUTCHER, S. E. 2005. Solution structure and thermodynamic
1242 investigation of the HIV-1 frameshift inducing element. *J Mol Biol,* 349**,** 1011-
1243 23.
1244 SUBRAMANIAN, A., TAMAYO, P., MOOTHA, V. K., MUKHERJEE, S., EBERT, B. L.,
1245 GILLETTE, M. A., PAULOVICH, A., POMEROY, S. L., GOLUB, T. R., LANDER, E. S.

1246 & MESIROV, J. P. 2005. Gene set enrichment analysis: a knowledge-based
1247 approach for interpreting genome-wide expression profiles. *Proc Natl Acad Sci*
1248 *U S A,* 102**,** 15545-50.
1249 TAYLOR, J. R., SKEATE, J. G. & KAST, W. M. 2018. Annexin A2 in Virus Infection. *Front*
1250 *Microbiol,* 9**,** 2954.
1251 TENENBAUM, D. 2020. KEGGREST: Client-side REST access to KEGG. R package
1252 version 1.6.4.
1253 WANG, X., XUAN, Y., HAN, Y., DING, X., YE, K., YANG, F., GAO, P., GOFF, S. P. & GAO, G.
1254 2019. Regulation of HIV-1 Gag-Pol Expression by Shiftless, an Inhibitor of
1255 Programmed -1 Ribosomal Frameshifting. *Cell,* 176**,** 625-635 e14.
1256 WEISS, S. R. & NAVAS-MARTIN, S. 2005. Coronavirus pathogenesis and the emerging
1257 pathogen severe acute respiratory syndrome coronavirus. *Microbiol Mol Biol*
1258 *Rev,* 69**,** 635-64.
1259 WILK, A. J., RUSTAGI, A., ZHAO, N. Q., ROQUE, J., MARTINEZ-COLON, G. J., MCKECHNIE,
1260 J. L., IVISON, G. T., RANGANATH, T., VERGARA, R., HOLLIS, T., SIMPSON, L. J.,
1261 GRANT, P., SUBRAMANIAN, A., ROGERS, A. J. & BLISH, C. A. 2020. A single-cell
1262 atlas of the peripheral immune response in patients with severe COVID-19.
1263 *Nat Med,* 26**,** 1070-1076.
1264 WILSON, W., BRADDOCK, M., ADAMS, S. E., RATHJEN, P. D., KINGSMAN, S. M. &
1265 KINGSMAN, A. J. 1988. HIV expression strategies: ribosomal frameshifting is
1266 directed by a short sequence in both mammalian and yeast systems. *Cell,* 55**,**
1267 1159-69.
1268 XIAO, H., XU, L. H., YAMADA, Y. & LIU, D. X. 2008. Coronavirus spike protein inhibits
1269 host cell translation by interaction with eIF3f. *PLoS One,* 3**,** e1494.
1270 XIE, X., MURUATO, A., LOKUGAMAGE, K. G., NARAYANAN, K., ZHANG, X., ZOU, J., LIU,
1271 J., SCHINDEWOLF, C., BOPP, N. E., AGUILAR, P. V., PLANTE, K. S., WEAVER, S. C.,
1272 MAKINO, S., LEDUC, J. W., MENACHERY, V. D. & SHI, P. Y. 2020. An Infectious
1273 cDNA Clone of SARS-CoV-2. *Cell Host Microbe,* 27**,** 841-848 e3.
1274 YOU, Y., RICHER, E. J., HUANG, T. & BRODY, S. L. 2002. Growth and differentiation of
1275 mouse tracheal epithelial cells: selection of a proliferative population. *Am J*
1276 *Physiol Lung Cell Mol Physiol,* 283**,** L1315-21.
1277 YOUNG, M. D., WAKEFIELD, M. J., SMYTH, G. K. & OSHLACK, A. 2010. Gene ontology
1278 analysis for RNA-seq: accounting for selection bias. *Genome Biol,* 11**,** R14.
1279 ZHANG, P., HE, D., XU, Y., HOU, J., PAN, B. F., WANG, Y., LIU, T., DAVIS, C. M., EHLI, E. A.,
1280 TAN, L., ZHOU, F., HU, J., YU, Y., CHEN, X., NGUYEN, T. M., ROSEN, J. M., HAWKE,
1281 D. H., JI, Z. & CHEN, Y. 2017. Genome-wide identification and differential
1282 analysis of translational initiation. *Nat Commun,* 8**,** 1749.
1283 ZHOU, B., LIU, J., WANG, Q., LIU, X., LI, X., LI, P., MA, Q. & CAO, C. 2008. The nucleocapsid
1284 protein of severe acute respiratory syndrome coronavirus inhibits cell
1285 cytokinesis and proliferation by interacting with translation elongation factor
1286 1alpha. *J Virol,* 82**,** 6962-71.
1287 ZHOU, Z., REN, L., ZHANG, L., ZHONG, J., XIAO, Y., JIA, Z., GUO, L., YANG, J., WANG, C.,
1288 JIANG, S., YANG, D., ZHANG, G., LI, H., CHEN, F., XU, Y., CHEN, M., GAO, Z., YANG,
1289 J., DONG, J., LIU, B., ZHANG, X., WANG, W., HE, K., JIN, Q., LI, M. & WANG, J. 2020.
1290 Heightened Innate Immune Responses in the Respiratory Tract of COVID-19
1291 Patients. *Cell Host Microbe,* 27**,** 883-890 e2.

1292

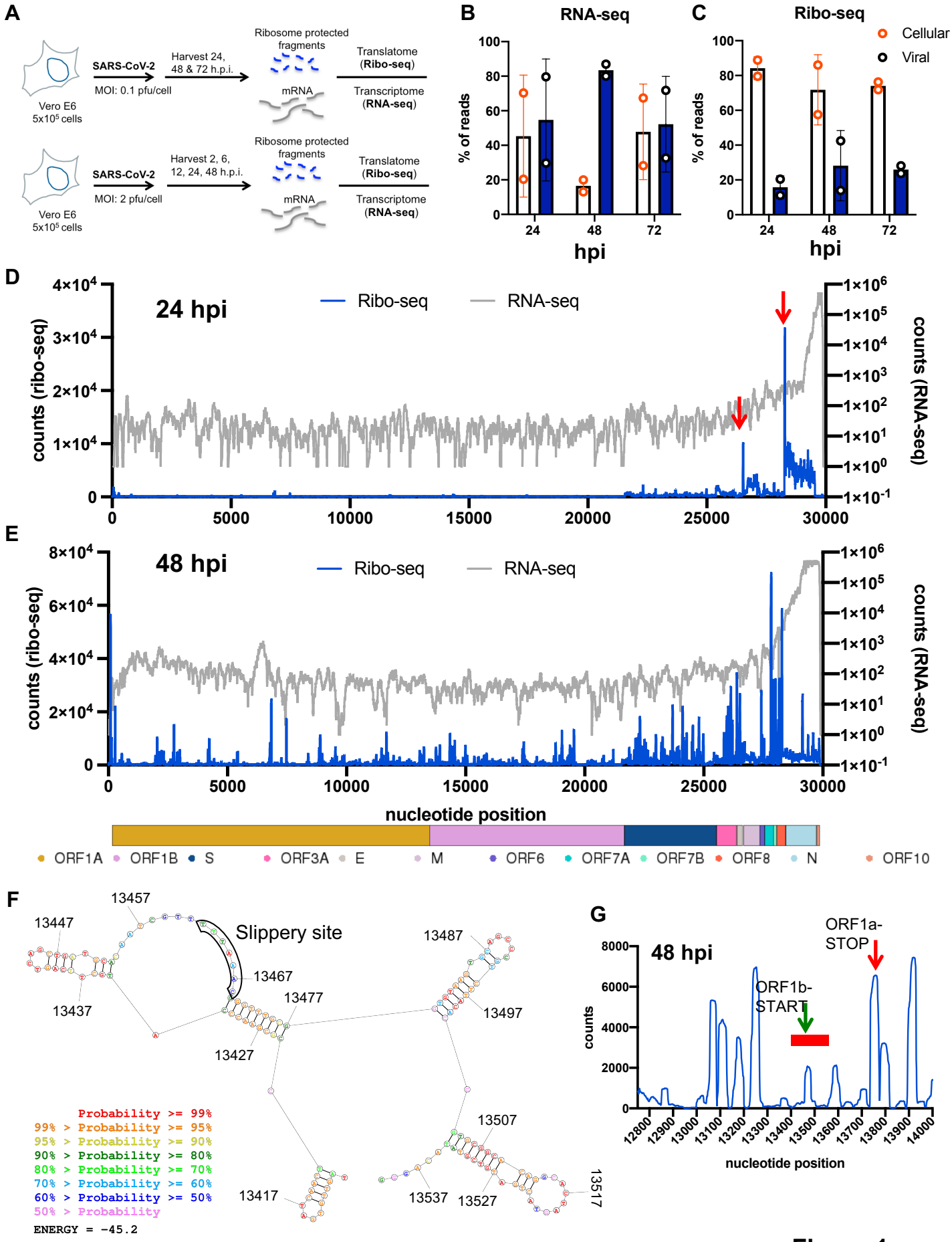
A
SARS-CoV-2
MOI: 0.1 pfu/cell
Harvest 24, 48 & 72 h.p.i.
Vero E6 5x10^5 cells
Ribosome protected fragments
mRNA
Translatome (Ribo-seq)
Transcriptome (RNA-seq)
SARS-CoV-2
MOI: 2 pfu/cell
Harvest 2, 6, 12, 24, 48 h.p.i.
Vero E6 5x10^5 cells
Ribosome protected fragments
mRNA
Translatome (Ribo-seq)
Transcriptome (RNA-seq)
B
RNA-seq
% of reads
hpi
C
Ribo-seq
Cellular
Viral
% of reads
hpi
D
24 hpi
Ribo-seq
RNA-seq
counts (ribo-seq)
counts (RNA-seq)
E
48 hpi
Ribo-seq
RNA-seq
counts (ribo-seq)
counts (RNA-seq)
nucleotide position
ORF1A
ORF1B
S
ORF3A
E
M
ORF6
ORF7A
ORF7B
ORF8
N
ORF10
F
Slippery site
13457
13447
13437
13467
13477
13427
13487
13497
13507
13517
13537
13527
13417
Probability >= 99%
99% > Probability >= 95%
95% > Probability >= 90%
90% > Probability >= 80%
80% > Probability >= 70%
70% > Probability >= 60%
60% > Probability >= 50%
50% > Probability
ENERGY = -45.2
G
48 hpi
ORF1a-STOP
ORF1b-START
counts
nucleotide position

Figure 1

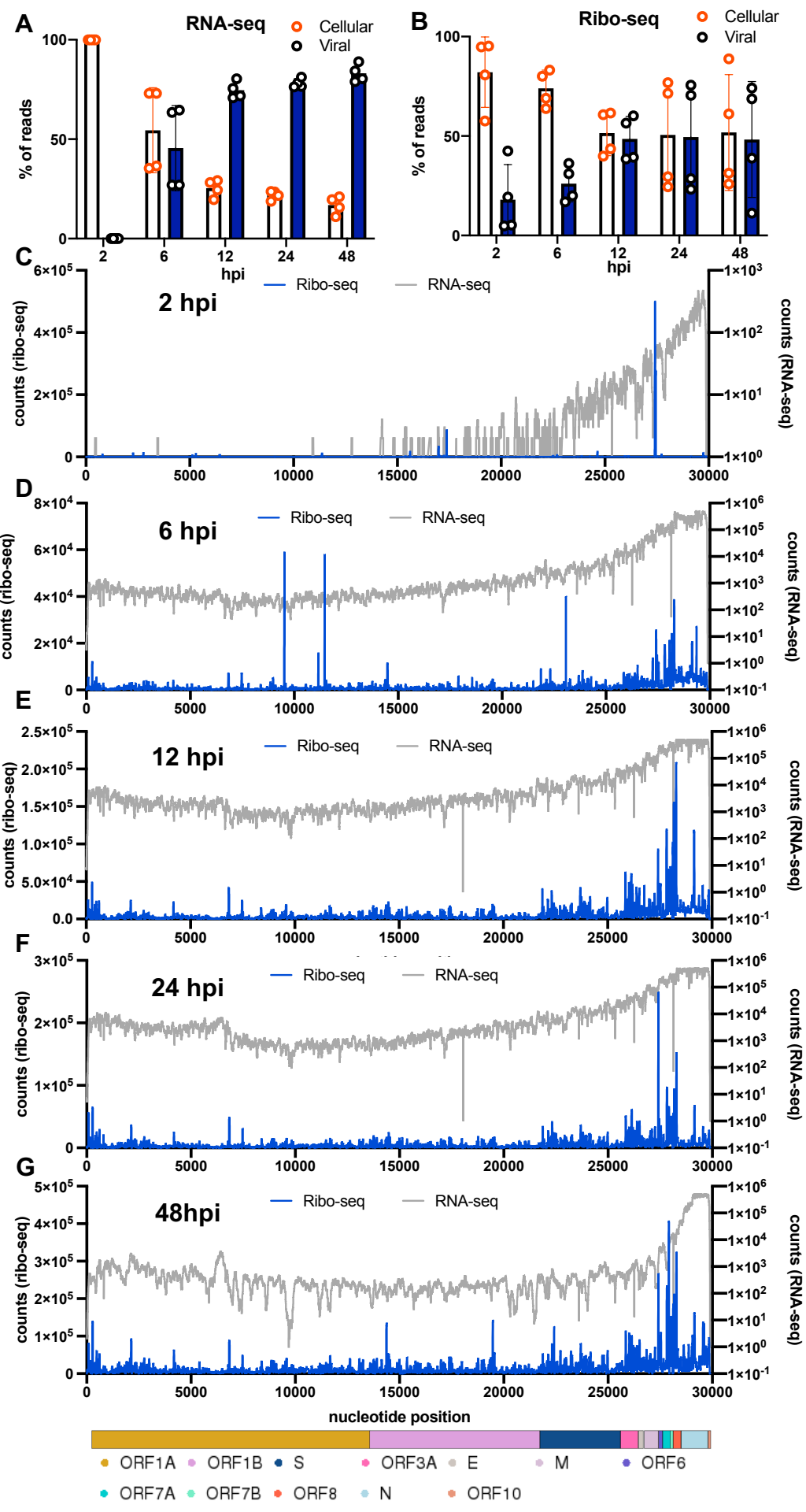
A
RNA-seq
Cellular
Viral
% of reads
hpi
B
Ribo-seq
Cellular
Viral
% of reads
hpi
C
2 hpi
Ribo-seq
RNA-seq
counts (ribo-seq)
counts (RNA-seq)
D
6 hpi
Ribo-seq
RNA-seq
counts (ribo-seq)
counts (RNA-seq)
E
12 hpi
Ribo-seq
RNA-seq
counts (ribo-seq)
counts (RNA-seq)
F
24 hpi
Ribo-seq
RNA-seq
counts (ribo-seq)
counts (RNA-seq)
G
48hpi
Ribo-seq
RNA-seq
counts (ribo-seq)
counts (RNA-seq)
nucleotide position
ORF1A
ORF1B
S
ORF3A
E
M
ORF6
ORF7A
ORF7B
ORF8
N
ORF10

Figure 2

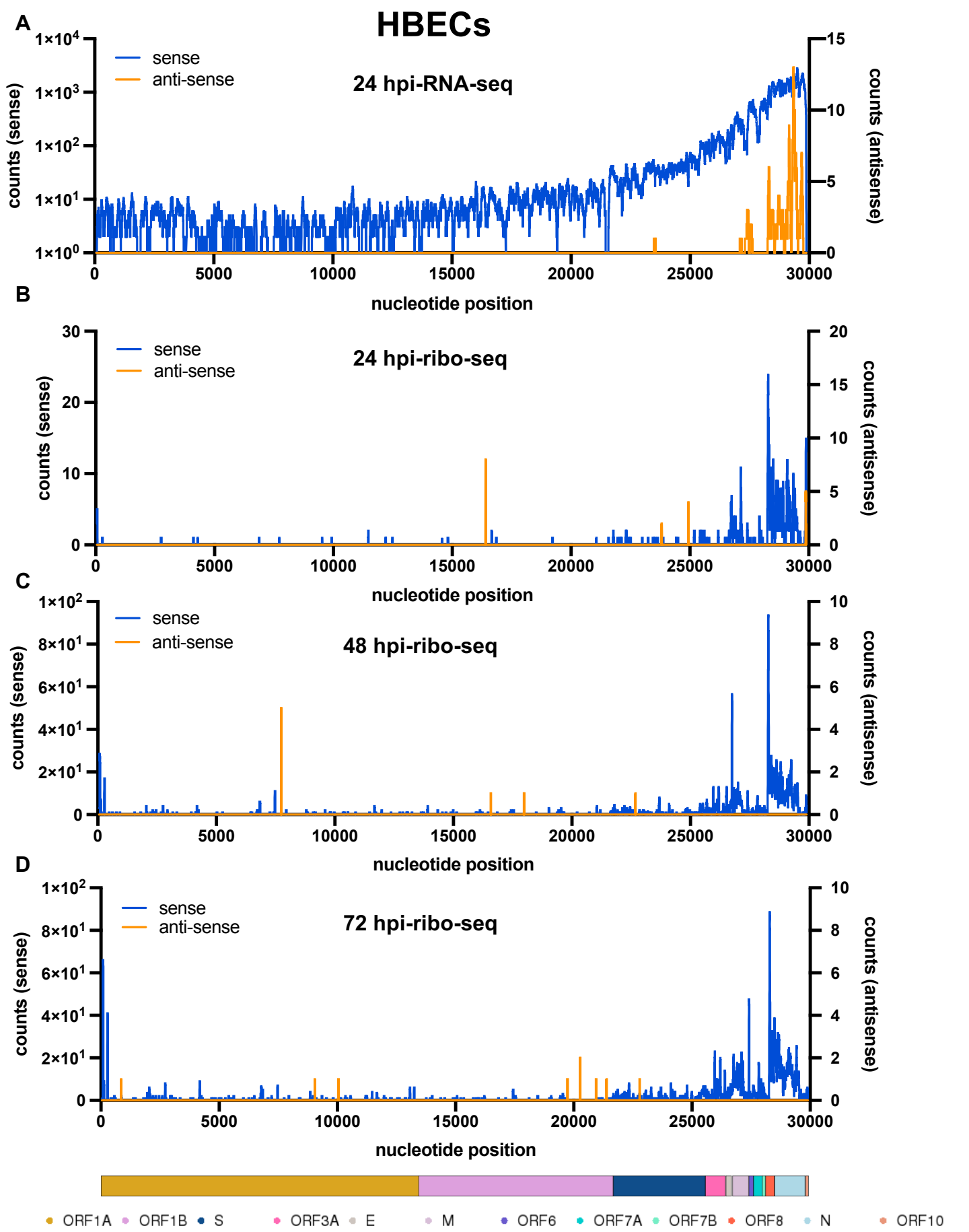
HBECs
A
24 hpi-RNA-seq
sense
anti-sense
counts (sense)
counts (antisense)
nucleotide position
B
24 hpi-ribo-seq
C
48 hpi-ribo-seq
D
72 hpi-ribo-seq
ORF1A
ORF1B
S
ORF3A
E
M
ORF6
ORF7A
ORF7B
ORF8
N
ORF10

Figure 3

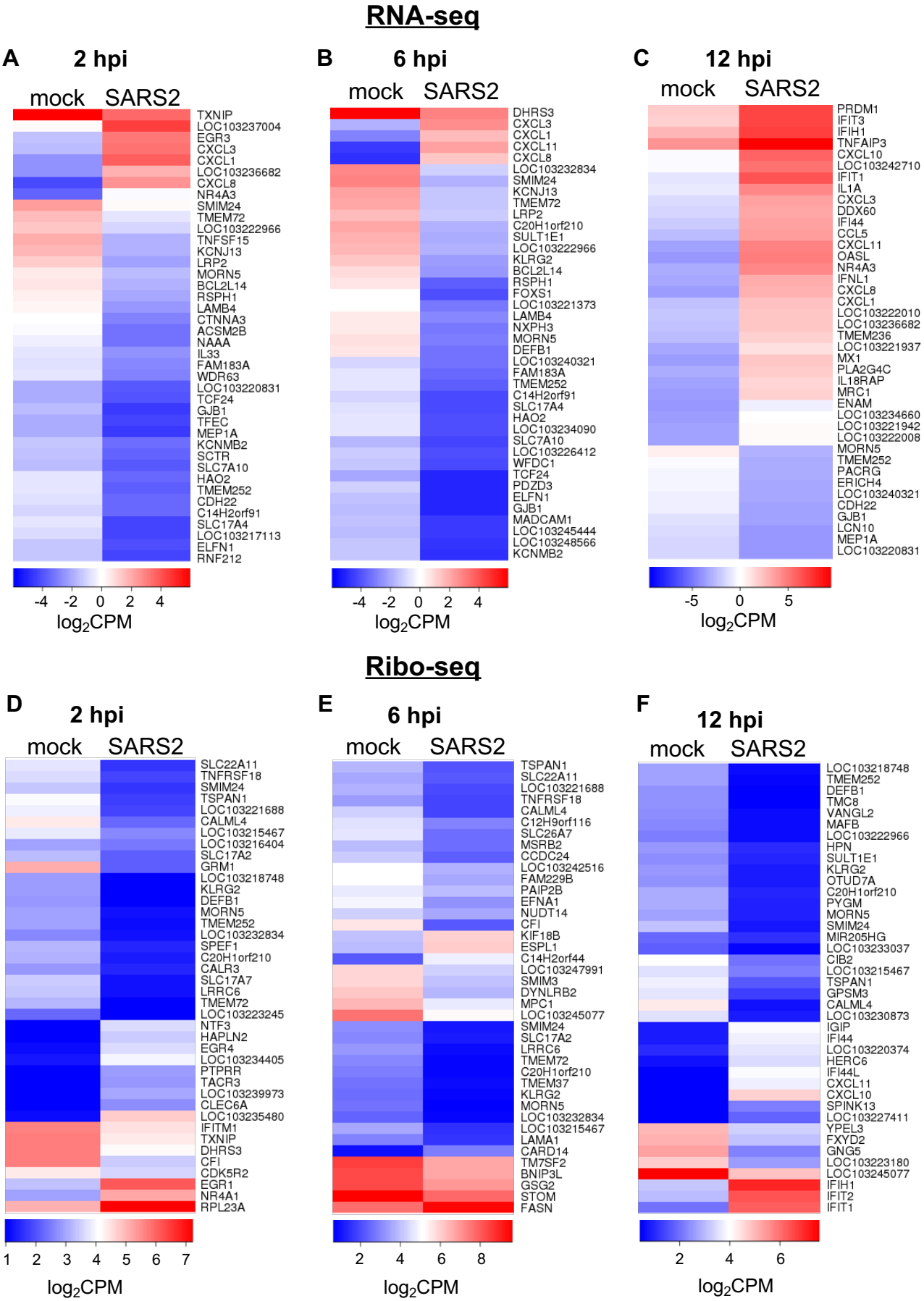
RNA-seq
A
2 hpi
mock
SARS2
TXNIP
LOC103237004
EGR3
CXCL3
CXCL1
LOC103236682
CXCL8
NR4A3
SMIM24
TMEM72
LOC103222966
TNFSF15
KCNJ13
LRP2
MORN5
BCL2L14
RSPH1
LAMB4
CTNNA3
ACSM2B
NAAA
IL33
FAM183A
WDR63
LOC103220831
TCF24
GJB1
TFEC
MEP1A
KCNMB2
SCTR
SLC7A10
HAO2
TMEM252
CDH22
C14H2orf91
SLC17A4
LOC103217113
ELFN1
RNF212
-4 -2 0 2 4
log2CPM
B
6 hpi
mock
SARS2
DHRS3
CXCL3
CXCL1
CXCL11
CXCL8
LOC103232834
SMIM24
KCNJ13
TMEM72
LRP2
C20H1orf210
SULT1E1
LOC103222966
KLRG2
BCL2L14
RSPH1
FOXS1
LOC103221373
LAMB4
NXPH3
MORN5
DEFB1
LOC103240321
FAM183A
TMEM252
C14H2orf91
SLC17A4
HAO2
LOC103234090
SLC7A10
LOC103226412
WFDC1
TCF24
PDZD3
ELFN1
GJB1
MADCAM1
LOC103245444
LOC103248566
KCNMB2
-4 -2 0 2 4
log2CPM
C
12 hpi
mock
SARS2
PRDM1
IFIT3
IFIH1
TNFAIP3
CXCL10
LOC103242710
IFIT1
IL1A
CXCL3
DDX60
IFI44
CCL5
CXCL11
OASL
NR4A3
IFNL1
CXCL8
CXCL1
LOC103222010
LOC103236682
TMEM236
LOC103221937
MX1
PLA2G4C
IL18RAP
MRC1
ENAM
LOC103234660
LOC103221942
LOC103222008
MORN5
TMEM252
PACRG
ERICH4
LOC103240321
CDH22
GJB1
LCN10
MEP1A
LOC103220831
-5 0 5
log2CPM
Ribo-seq
D
2 hpi
mock
SARS2
SLC22A11
TNFRSF18
SMIM24
TSPAN1
LOC103221688
CALML4
LOC103215467
LOC103216404
SLC17A2
GRM1
LOC103218748
KLRG2
DEFB1
MORN5
TMEM252
LOC103232834
SPEF1
C20H1orf210
CALR3
SLC17A7
LRRC6
TMEM72
LOC103223245
NTF3
HAPLN2
EGR4
LOC103234405
PTPRR
TACR3
LOC103239973
CLEC6A
LOC103235480
IFITM1
TXNIP
DHRS3
CFI
CDK5R2
EGR1
NR4A1
RPL23A
1 2 3 4 5 6 7
log2CPM
E
6 hpi
mock
SARS2
TSPAN1
SLC22A11
LOC103221688
TNFRSF18
CALML4
C12H9orf116
SLC26A7
MSRB2
CCDC24
LOC103242516
FAM229B
PAIP2B
EFNA1
NUDT14
CFI
KIF18B
ESPL1
C14H2orf44
LOC103247991
SMIM3
DYNLRB2
MPC1
LOC103245077
SMIM24
SLC17A2
LRRC6
TMEM72
C20H1orf210
TMEM37
KLRG2
MORN5
LOC103232834
LOC103215467
LAMA1
CARD14
TM7SF2
BNIP3L
GSG2
STOM
FASN
2 4 6 8
log2CPM
F
12 hpi
mock
SARS2
LOC103218748
TMEM252
DEFB1
TMC8
VANGL2
MAFB
LOC103222966
HPN
SULT1E1
KLRG2
OTUD7A
C20H1orf210
PYGM
MORN5
SMIM24
MIR205HG
LOC103233037
CIB2
LOC103215467
TSPAN1
GPSM3
CALML4
LOC103230873
IGIP
IFI44
LOC103220374
HERC6
IFI44L
CXCL11
CXCL10
SPINK13
LOC103227411
YPEL3
FXYD2
GNG5
LOC103223180
LOC103245077
IFIH1
IFIT2
IFIT1
2 4 6
log2CPM

Figure 4

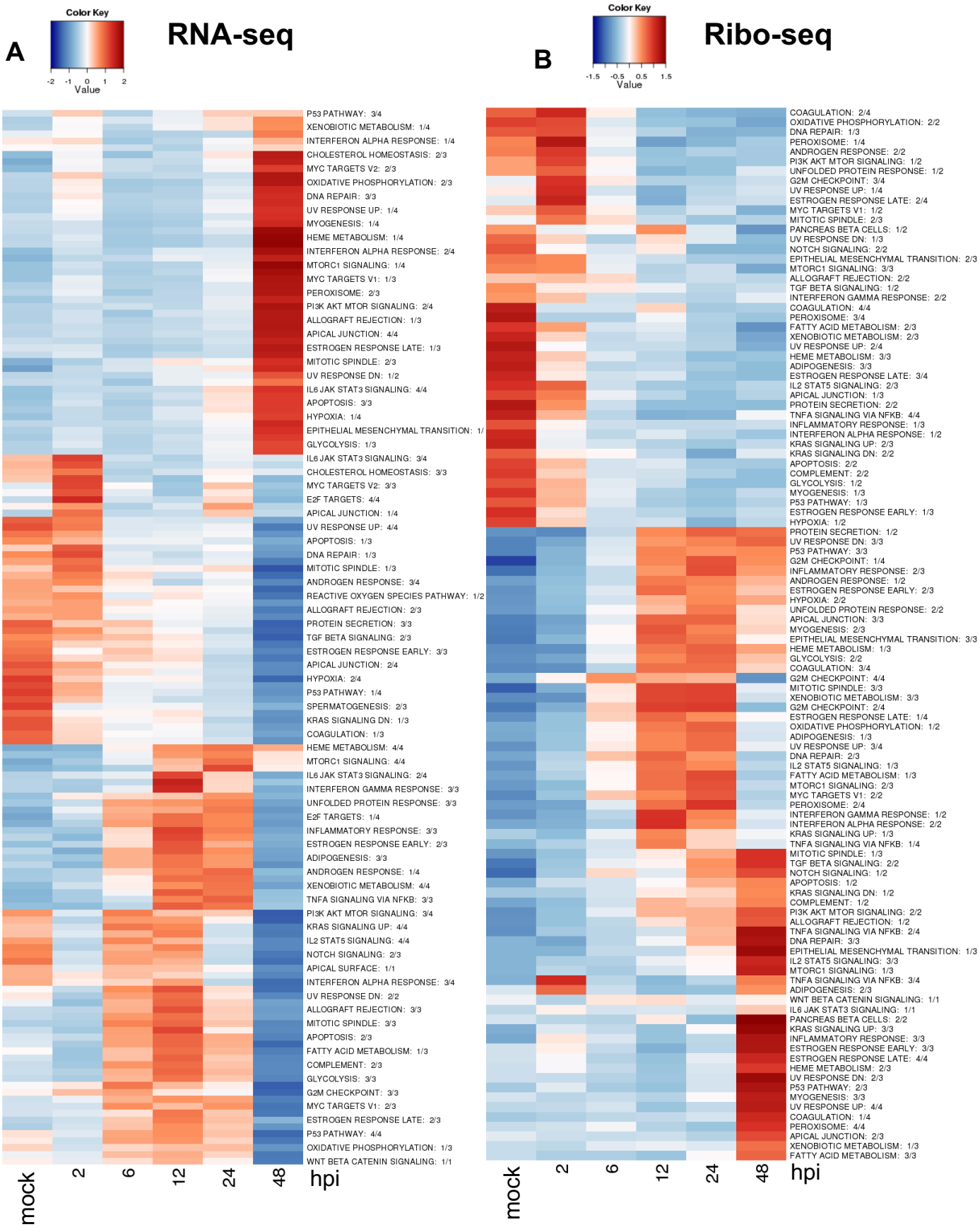
A
Color Key
-2 -1 0 1 2
Value
RNA-seq
P53 PATHWAY: 3/4
XENOBIOTIC METABOLISM: 1/4
INTERFERON ALPHA RESPONSE: 1/4
CHOLESTEROL HOMEOSTASIS: 2/3
MYC TARGETS V2: 2/3
OXIDATIVE PHOSPHORYLATION: 2/3
DNA REPAIR: 3/3
UV RESPONSE UP: 1/4
MYOGENESIS: 1/4
HEME METABOLISM: 1/4
INTERFERON ALPHA RESPONSE: 2/4
MTORC1 SIGNALING: 1/4
MYC TARGETS V1: 1/3
PEROXISOME: 2/3
PI3K AKT MTOR SIGNALING: 2/4
ALLOGRAFT REJECTION: 1/3
APICAL JUNCTION: 4/4
ESTROGEN RESPONSE LATE: 1/3
MITOTIC SPINDLE: 2/3
UV RESPONSE DN: 1/2
IL6 JAK STAT3 SIGNALING: 4/4
APOPTOSIS: 3/3
HYPOXIA: 1/4
EPITHELIAL MESENCHYMAL TRANSITION: 1/
GLYCOLYSIS: 1/3
IL6 JAK STAT3 SIGNALING: 3/4
CHOLESTEROL HOMEOSTASIS: 3/3
MYC TARGETS V2: 3/3
E2F TARGETS: 4/4
APICAL JUNCTION: 1/4
UV RESPONSE UP: 4/4
APOPTOSIS: 1/3
DNA REPAIR: 1/3
MITOTIC SPINDLE: 1/3
ANDROGEN RESPONSE: 3/4
REACTIVE OXYGEN SPECIES PATHWAY: 1/2
ALLOGRAFT REJECTION: 2/3
PROTEIN SECRETION: 3/3
TGF BETA SIGNALING: 2/3
ESTROGEN RESPONSE EARLY: 3/3
APICAL JUNCTION: 2/4
HYPOXIA: 2/4
P53 PATHWAY: 1/4
SPERMATOGENESIS: 2/3
KRAS SIGNALING DN: 1/3
COAGULATION: 1/3
HEME METABOLISM: 4/4
MTORC1 SIGNALING: 4/4
IL6 JAK STAT3 SIGNALING: 2/4
INTERFERON GAMMA RESPONSE: 3/3
UNFOLDED PROTEIN RESPONSE: 3/3
E2F TARGETS: 1/4
INFLAMMATORY RESPONSE: 3/3
ESTROGEN RESPONSE EARLY: 2/3
ADIPOGENESIS: 3/3
ANDROGEN RESPONSE: 1/4
XENOBIOTIC METABOLISM: 4/4
TNFA SIGNALING VIA NFKB: 3/3
PI3K AKT MTOR SIGNALING: 3/4
KRAS SIGNALING UP: 4/4
IL2 STAT5 SIGNALING: 4/4
NOTCH SIGNALING: 2/3
APICAL SURFACE: 1/1
INTERFERON ALPHA RESPONSE: 3/4
UV RESPONSE DN: 2/2
ALLOGRAFT REJECTION: 3/3
MITOTIC SPINDLE: 3/3
APOPTOSIS: 2/3
FATTY ACID METABOLISM: 1/3
COMPLEMENT: 2/3
GLYCOLYSIS: 3/3
G2M CHECKPOINT: 3/3
MYC TARGETS V1: 2/3
ESTROGEN RESPONSE LATE: 2/3
P53 PATHWAY: 4/4
OXIDATIVE PHOSPHORYLATION: 1/3
WNT BETA CATENIN SIGNALING: 1/1
mock
2
6
12
24
48
hpi
B
Color Key
-1.5 -0.5 0.5 1.5
Value
Ribo-seq
COAGULATION: 2/4
OXIDATIVE PHOSPHORYLATION: 2/2
DNA REPAIR: 1/3
PEROXISOME: 1/4
ANDROGEN RESPONSE: 2/2
PI3K AKT MTOR SIGNALING: 1/2
UNFOLDED PROTEIN RESPONSE: 1/2
G2M CHECKPOINT: 3/4
UV RESPONSE UP: 1/4
ESTROGEN RESPONSE LATE: 2/4
MYC TARGETS V1: 1/2
MITOTIC SPINDLE: 2/3
PANCREAS BETA CELLS: 1/2
UV RESPONSE DN: 1/3
NOTCH SIGNALING: 2/2
EPITHELIAL MESENCHYMAL TRANSITION: 2/3
MTORC1 SIGNALING: 3/3
ALLOGRAFT REJECTION: 2/2
TGF BETA SIGNALING: 1/2
INTERFERON GAMMA RESPONSE: 2/2
COAGULATION: 4/4
PEROXISOME: 3/4
FATTY ACID METABOLISM: 2/3
XENOBIOTIC METABOLISM: 2/3
UV RESPONSE UP: 2/4
HEME METABOLISM: 3/3
ADIPOGENESIS: 3/3
ESTROGEN RESPONSE LATE: 3/4
IL2 STAT5 SIGNALING: 2/3
APICAL JUNCTION: 1/3
PROTEIN SECRETION: 2/2
TNFA SIGNALING VIA NFKB: 4/4
INFLAMMATORY RESPONSE: 1/3
INTERFERON ALPHA RESPONSE: 1/2
KRAS SIGNALING UP: 2/3
KRAS SIGNALING DN: 2/2
APOPTOSIS: 2/2
COMPLEMENT: 2/2
GLYCOLYSIS: 1/2
MYOGENESIS: 1/3
P53 PATHWAY: 1/3
ESTROGEN RESPONSE EARLY: 1/3
HYPOXIA: 1/2
PROTEIN SECRETION: 1/2
UV RESPONSE DN: 3/3
P53 PATHWAY: 3/3
G2M CHECKPOINT: 1/4
INFLAMMATORY RESPONSE: 2/3
ANDROGEN RESPONSE: 1/2
ESTROGEN RESPONSE EARLY: 2/3
HYPOXIA: 2/2
UNFOLDED PROTEIN RESPONSE: 2/2
APICAL JUNCTION: 3/3
MYOGENESIS: 2/3
EPITHELIAL MESENCHYMAL TRANSITION: 3/3
HEME METABOLISM: 1/3
GLYCOLYSIS: 2/2
COAGULATION: 3/4
G2M CHECKPOINT: 4/4
MITOTIC SPINDLE: 3/3
XENOBIOTIC METABOLISM: 3/3
G2M CHECKPOINT: 2/4
ESTROGEN RESPONSE LATE: 1/4
OXIDATIVE PHOSPHORYLATION: 1/2
ADIPOGENESIS: 1/3
UV RESPONSE UP: 3/4
DNA REPAIR: 2/3
IL2 STAT5 SIGNALING: 1/3
FATTY ACID METABOLISM: 1/3
MTORC1 SIGNALING: 2/3
MYC TARGETS V1: 2/2
PEROXISOME: 2/4
INTERFERON GAMMA RESPONSE: 1/2
INTERFERON ALPHA RESPONSE: 2/2
KRAS SIGNALING UP: 1/3
TNFA SIGNALING VIA NFKB: 1/4
MITOTIC SPINDLE: 1/3
TGF BETA SIGNALING: 2/2
NOTCH SIGNALING: 1/2
APOPTOSIS: 1/2
KRAS SIGNALING DN: 1/2
COMPLEMENT: 1/2
PI3K AKT MTOR SIGNALING: 2/2
ALLOGRAFT REJECTION: 1/2
TNFA SIGNALING VIA NFKB: 2/4
DNA REPAIR: 3/3
EPITHELIAL MESENCHYMAL TRANSITION: 1/3
IL2 STAT5 SIGNALING: 3/3
MTORC1 SIGNALING: 1/3
TNFA SIGNALING VIA NFKB: 3/4
ADIPOGENESIS: 2/3
WNT BETA CATENIN SIGNALING: 1/1
IL6 JAK STAT3 SIGNALING: 1/1
PANCREAS BETA CELLS: 2/2
KRAS SIGNALING UP: 3/3
INFLAMMATORY RESPONSE: 3/3
ESTROGEN RESPONSE EARLY: 3/3
ESTROGEN RESPONSE LATE: 4/4
HEME METABOLISM: 2/3
UV RESPONSE DN: 2/3
P53 PATHWAY: 2/3
MYOGENESIS: 3/3
UV RESPONSE UP: 4/4
COAGULATION: 1/4
PEROXISOME: 4/4
APICAL JUNCTION: 2/3
XENOBIOTIC METABOLISM: 1/3
FATTY ACID METABOLISM: 3/3
mock
2
6
12
24
48
hpi

Figure 5

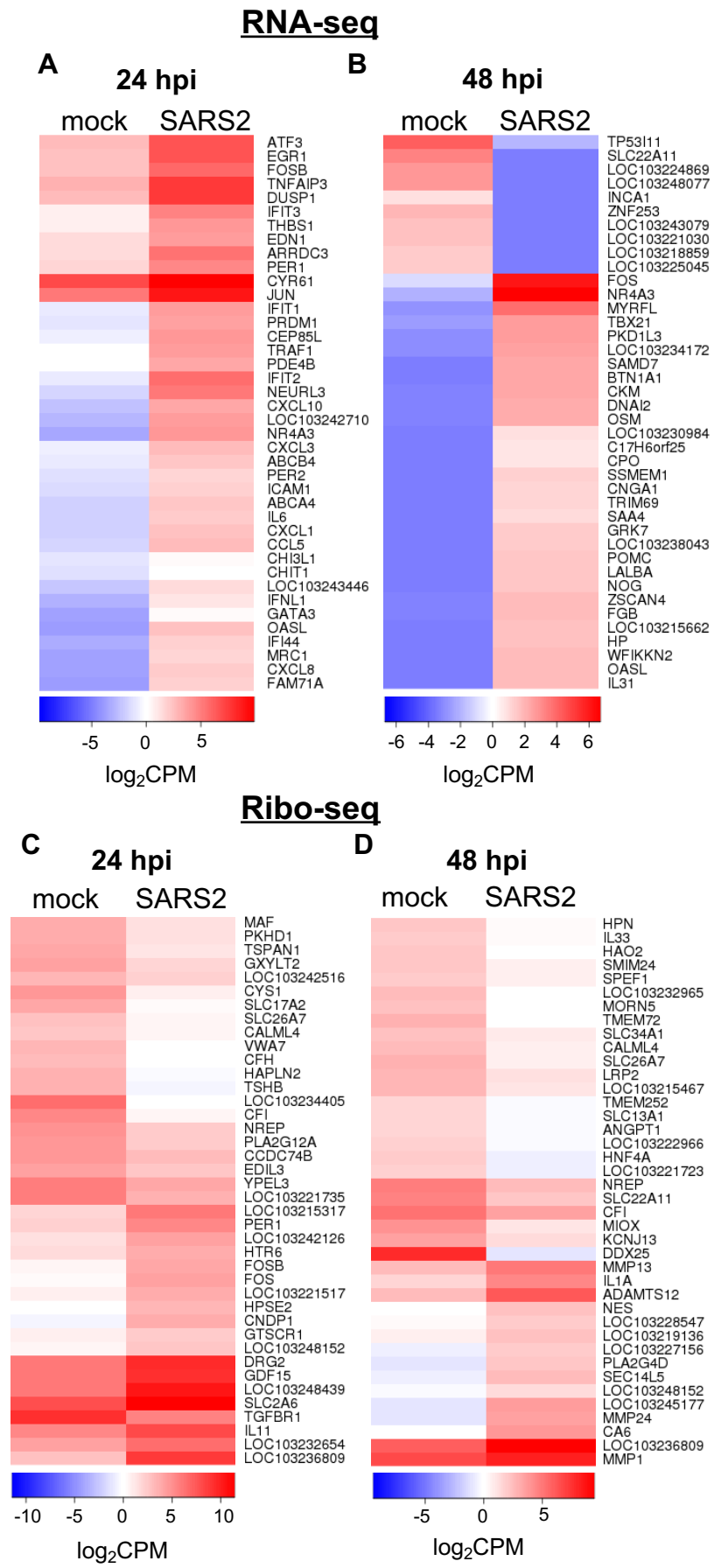
RNA-seq
A
24 hpi
mock
SARS2
ATF3
EGR1
FOSB
TNFAIP3
DUSP1
IFIT3
THBS1
EDN1
ARRDC3
PER1
CYR61
JUN
IFIT1
PRDM1
CEP85L
TRAF1
PDE4B
IFIT2
NEURL3
CXCL10
LOC103242710
NR4A3
CXCL3
ABCB4
PER2
ICAM1
ABCA4
IL6
CXCL1
CCL5
CHI3L1
CHIT1
LOC103243446
IFNL1
GATA3
OASL
IFI44
MRC1
CXCL8
FAM71A
-5 0 5
log2CPM
B
48 hpi
mock
SARS2
TP53I11
SLC22A11
LOC103224869
LOC103248077
INCA1
ZNF253
LOC103243079
LOC103221030
LOC103218859
LOC103225045
FOS
NR4A3
MYRFL
TBX21
PKD1L3
LOC103234172
SAMD7
BTN1A1
CKM
DNAI2
OSM
LOC103230984
C17H6orf25
CPO
SSMEM1
CNGA1
TRIM69
SAA4
GRK7
LOC103238043
POMC
LALBA
NOG
ZSCAN4
FGB
LOC103215662
HP
WFIKKN2
OASL
IL31
-6 -4 -2 0 2 4 6
log2CPM
Ribo-seq
C
24 hpi
mock
SARS2
MAF
PKHD1
TSPAN1
GXYLT2
LOC103242516
CYS1
SLC17A2
SLC26A7
CALML4
VWA7
CFH
HAPLN2
TSHB
LOC103234405
CFI
NREP
PLA2G12A
CCDC74B
EDIL3
YPEL3
LOC103221735
LOC103215317
PER1
LOC103242126
HTR6
FOSB
FOS
LOC103221517
HPSE2
CNDP1
GTSCR1
LOC103248152
DRG2
GDF15
LOC103248439
SLC2A6
TGFBR1
IL11
LOC103232654
LOC103236809
-10 -5 0 5 10
log2CPM
D
48 hpi
mock
SARS2
HPN
IL33
HAO2
SMIM24
SPEF1
LOC103232965
MORN5
TMEM72
SLC34A1
CALML4
SLC26A7
LRP2
LOC103215467
TMEM252
SLC13A1
ANGPT1
LOC103222966
HNF4A
LOC103221723
NREP
SLC22A11
CFI
MIOX
KCNJ13
DDX25
MMP13
IL1A
ADAMTS12
NES
LOC103228547
LOC103219136
LOC103227156
PLA2G4D
SEC14L5
LOC103248152
LOC103245177
MMP24
CA6
LOC103236809
MMP1
-5 0 5
log2CPM

Figure 6

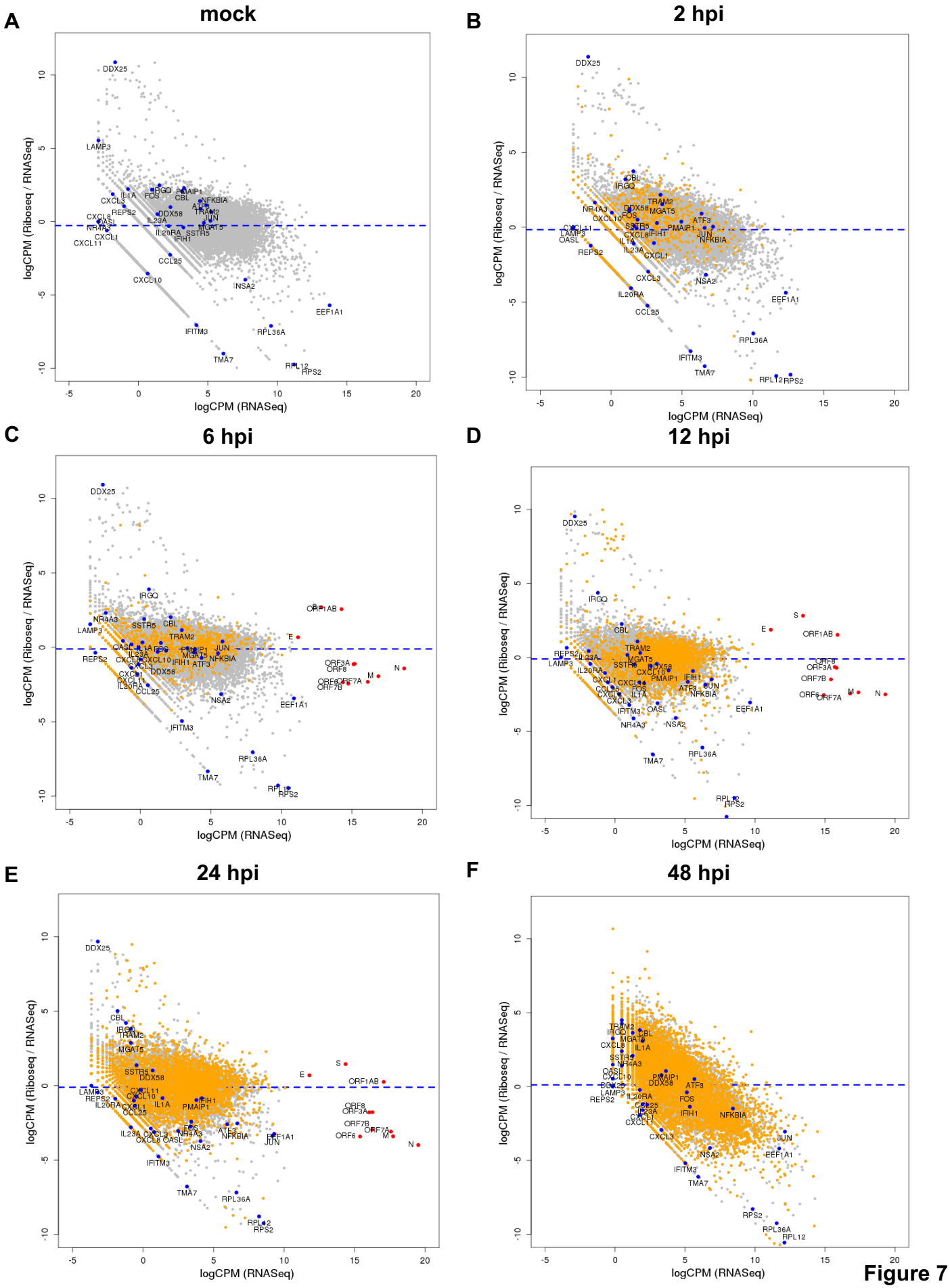
A
mock
B
2 hpi
C
6 hpi
D
12 hpi
E
24 hpi
F
48 hpi
logCPM (Riboseq / RNASeq)
logCPM (RNASeq)

Figure 7